THESIS FOR THE DEGREE OF LICENTIATE OF ENGINEERING

Structure and Thermoelectric Properties of Type-I Clathrates $Ba_8(Al_xGa_{1-x})_{16}Ge_{30}$

Yifei Zhang

Department of Chemistry and Chemical Engineering
Division of Applied Chemistry
CHALMERS UNIVERSITY OF TECHNOLOGY

Göteborg, Sweden 2020

Structure and Thermoelectric Properties of Type-I Clathrates $Ba_8(Al_xGa_{1-x})_{16}Ge_{30}$
YIFEI ZHANG

Licentiatuppsatser vid institutionen för kemi och kemiteknik
Chalmers tekniska högskola
Nr 2020:16

Division of Applied Chemistry
Department of Chemistry and Chemical Engineering
Chalmers University of Technology
SE-412 96 Göteborg
Sweden
Telephone: +46 (0)31-772 1000

Cover
Crystal structure of type-I clathrates. Art by Joakim Brorsson.

Printed by Chalmers Reproservice
Göteborg, Sweden 2020

Abstract

Thermoelectric materials enable the direct conversion between a thermal gradient and an electrical potential gradient, and can thus be exploited for electricity generation. One of the promising thermoelectric materials is type-I clathrates. They are regarded as realizations of the phonon-glass electron-crystal concept, combining relatively large electrical conductivity with very low thermal conductivity. However, a moderate power factor renders room for further improvement, and the role of the complex atomic structure has not been fully understood. This thesis studies the thermoelectric properties of type-I clathrate $Ba_8(Al_xGa_{1-x})_{16}Ge_{30}$ and investigates the impact of structure on the electron and phonon transport.

The power factor of clathrates is improved by modulation doping by introducing analogous compound $Ba_8Al_{16}Ge_{30}$ to the matrix phase $Ba_8Ga_{16}Ge_{30}$. A heterogeneous microstructure is created in the materials, which are composed of a Ga-rich clathrate matrix phase and Al particles. The charge carriers transfer from the latter to the former phase without lowering the charge carrier mobility, as compared to homogeneously doped materials. As a result of modulation doping, the carrier concentration and carrier mobility increase simultaneously. Especially, the carrier mobility is enhanced to a value that exceeds that reported for a single crystal with the same composition. Consequently, the highest figure of merit (zT) is achieved for $Ba_8(Al_{0.25}Ga_{0.75})_{16}Ge_{30}$, with the maximum value reaching 0.93 at 800 °C.

The atomic structure of quaternary $Ba_8(Al_xGa_{1-x})_{16}Ge_{30}$ is studied by the combination of X-ray and neutron diffraction. The obtained chemical ordering is validated and consistent with theoretical calculations. It is found that depending on the synthesis method, the trivalent elements Al and Ga show different occupation in the host framework. In turn, the atomic displacement parameter of the guest atoms in the larger tetrakaidecahedral cages is influenced by chemical ordering: the guest atoms are either localized at the center of the cage or moving towards the boundary of the cage periphery.

Keywords: Thermoelectrics, Clathrates, Microstructure, Crystal structure, Transport properties

List of Publications

This thesis is based on the following appended papers

Paper I:
Enhanced Thermoelectric Performance of $Ba_8Ga_{16}Ge_{30}$ Clathrate by Modulation Doping and Improved Carrier Mobility
Yifei Zhang, Joakim Brorsson, Ren Qiu, Anders E. C. Palmqvist
Submitted and reviewed by Advanced Electronic Materials

Paper II:
Investigating the Chemical Ordering in Quaternary Type-I Clathrates $Ba_8(Al_xGa_{1-x})_{16}Ge_{30}$
Yifei Zhang, Joakim Brorsson, Paul Erhart, Takashi Kamiyama, Anders E. C. Palmqvist
Manuscript

My Contribution

Paper I:
Responsible for experiments and writing the manuscript.

Paper II:
Responsible for most experiments except the synthesis of Czochralski sample and writing the manuscript.

List of Figures

List of Physical Properties and Abbreviations

C_p specific heat capacity.

κ thermal conductivity.

κ_e electronic thermal conductivity.

κ_l lattice thermal conductivity.

μ carrier mobility.

ρ electrical resistivity.

σ electrical conductivity.

F_{hkl} structure factor.

PF power factor.

S Seebeck coefficient.

e carrier charge.

n carrier concentration.

zT figure of merit.

m^* effective mass.

ADP atomic displacement parameter.

EDX energy-dispersive X-ray fluorescence analysis.

PGEC phonon-glass electron-crystal.

SEM scanning electron microscopy.

SPS spark plasma sintering.

TCR temperature coefficient of resistivity.

WDX wavelength-dispersive X-ray fluorescence analysis.

XRD X-ray diffraction.

XRF X-ray fluorescence analysis.

Contents

1 Introduction

The 21st Century will become the most important and most challenging century in human history. During the upcoming decades, humanity will face many unprecedented problems: climate change, depletion of fossil fuel, and air pollution to name a few. The broad societal needs have led to technologies that utilize renewable energy. According to the International Energy Agency, in 2017 the total energy loss in Europe was about 400 TWh, approximately 20 % was lost in the form of waste heat.[1] Thermoelectric devices can recover waste heat and convert it into electrical power, so are increasingly being seen as complement to reduce CO_2 and greenhouse gas emission and to provide cleaner form of energy.[2] The application of thermoelectric devices can be categorized depending on the working temperature: Bi_2Te_3-based room temperature ($<$ 100 °C), PbTe-based medium temperature (300 - 600 °C) and SiGe-based high temperature ($>$ 600 °C).[3–7] The room-temperature thermoelectric devices usually convert electricity into thermal energy for active cooling. One of the commercial products is Climate Control Seat, which is the first solid-state system to deliver seat cooling using thermoelectric materials.[2] Recent development of organic thermoelectric materials has opened a world of room-temperature applications, such as flexible and wearable electronics, which utilize a temperature difference of few degrees between human skin and air.[8] These organic materials are usually synthesized in solution, so the processing is scalable and cost-effective. High-temperature thermoelectric applications mainly refer to Radioisotope Thermoelectric Generators (RTGs), which have long been used as power sources in satellites and space probes.[8] In particular, 23 years after the production of RTGs in spacecraft Voyager, the power output still remained 80 % of its initial design, evidencing the robustness of the thermoelectric materials.[9]
As for the medium-temperature range, large amounts of energies are lost as waste heat, including combustion engines in vehicles, power stations, industrial plants like oil refineries and steel-making plants.[8] Recovering the waste heat by thermoelectric devices seems to be very attractive and economical. However, unlike other thermoelectric applications which find their unique market share or provide the exclusive energy choice, the medium-temperature devices are not that successful. The low efficiency is the major obstacle for thermoelectric materials, as compared to other materials for exploiting renewable energy sources, for instance photovoltaics and fuel cells. In addition, the state-of-art medium-temperature material PbTe contains toxic (Pb) and scarce (Te) elements,

which also hinders mass production. Improving the thermoelectric efficiency, as well as finding materials containing non-toxic and abundant elements, is the future for thermoelectrics.[10]
One of the promising materials is inorganic clathrates.[3] They are semiconductor materials exhibiting unique crystal structure, with nanosized cages that contain guest atoms, ions or molecules. Clathrates possess intrinsically low thermal conductivity, which is close to the amorphous limit. The fairly self-contradictory characteristic makes clathrates especially interesting for thermoelectric applications.[11–14]
This thesis is divided into two studies. The first study introduces an analogous compound to the clathrate matrix phase, studying the effect of microstructure on the thermoelectric properties. The second one studies the atomic structure of quaternary clathrate $Ba_8(Al_xGa_{1-x})_{16}Ge_{30}$ and investigates the chemical ordering in the host cage.

2 Background

2.1 Thermoelectric effects

Thermoelectric effects enable the direct conversion between a temperature difference and an electrical voltage, and encompasses three different effects: Seebeck effect, Peltier effect and Thomson effect.[15]
Seebeck effect, which was discovered by German physicist Thomas Johann Seebeck in 1821, is the ability of converting a temperature difference into electricity. As illustrated in Figure 2.1a, a thermoelectric power generator consists of both n- and p-type semiconductors, which are connected electrically in series and thermally in parallel. When applying a temperature gradient to these semiconductors, both the electrons (n-type) and holes (p-type) move from the hot side to the cold side, thus inducing an electric current in the power generator.
Conversely, Peltier effect describes the opposite phenomenon, where an electric potential creates a thermal gradient. Therefore, it can be used as thermoelectric refrigeration, as is shown in Figure 2.1b. Thomson effect relates to the generation of reversible heat, which originates from an electric current created by a temperature gradient along a single conductor. In other words, Thomson effect relates the two other effects, concluding that both are characterized by one key property, the Seebeck coefficient (S).

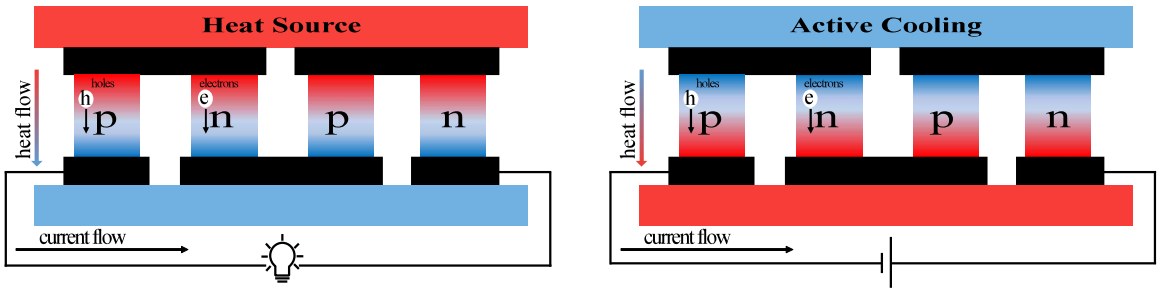

(a) (b)

Figure 2.1: *Illustration of thermoelectric devices: (a) power generator and (b) active cooler.*

2.2 Thermoelectric properties

2.2.1 Thermoelectric efficiency and figure of merit

The thermoelectric conversion efficiency (η) of a device is given in Equation 2.1 and can be obtained from the Carnot efficiency, which defines the maximum thermodynamic limit for the energy conversion, and a factor including the dimensionless figure of merit (zT), which describes the thermoelectric performance of a material:[15]

$$\eta = \frac{T_h - T_c}{T_h} \cdot \frac{\sqrt{1+zT}-1}{\sqrt{1+zT}+\frac{T_c}{T_h}} \tag{2.1}$$

where T_h and T_c refer to the temperature on the hot side and the cold side, respectively.
The thermoelectric figure of merit zT is defined as

$$zT = \frac{S^2 \cdot \sigma}{\kappa} \cdot T \tag{2.2}$$

and comprises three materials parameters: Seebeck coefficient (S) measures the strength of the coupling between thermal gradient and potential gradient, while σ and κ denote electrical and thermal conductivity, respectively.

2.2.2 Seebeck coefficient

Seebeck coefficient is defined as the magnitude of a thermoelectric voltage induced by a thermal gradient across the material, shows negative value for n-type semiconductors and positive for the p-type:

$$S = -\frac{\triangle V}{\triangle T} \tag{2.3}$$

The use of a material with high absolute Seebeck coefficient is one of the most important factors for efficient thermoelectric application. Nevertheless, increasing Seebeck coefficient is not straightforward, since it is dependent on the band structure of the materials.[16] There exist strategies to enhance the Seebeck coefficient solely, mainly by manipulating the band structure near the Fermi level, for instance through resonant states and band convergence.[16, 17]
On the other hand, for most metals or heavily doped semiconductors (usually thermoelectric materials are heavily doped semiconductors), parabolic band and energy-independent scattering approximation can be assumed,[3] thus the Seebeck coefficient is given by:

$$S = \frac{8\pi^2 k_B^2}{3e} m^* T \left(\frac{\pi}{n}\right)^{2/3} \tag{2.4}$$

where k_B and e are Boltzmann constant and carrier charge, m^* and n refer to the effective mass of the charge carrier and carrier concentration, respectively.

2.2.3 Electrical conductivity

Electrical conductivity (σ) and resistivity (ρ) are determined by the carrier concentration and carrier mobility (μ):

$$\sigma = 1/\rho = ne\mu \tag{2.5}$$

The carrier concentration can be tuned by doping, while the mobility is determined by the scattering mechanism of the charge carrier, including ionized impurity scattering, phonon scattering and alloy scattering.[18]

2.2.4 Thermal conductivity

Thermal conductivity describes the ability of a material to conduct heat. In solid materials, heat is usually carried by electrons and phonons:

$$\kappa = \kappa_e + \kappa_l \tag{2.6}$$

The thermal conductivity thus comprises both electronic κ_e and phononic (lattice) κ_l contributions. The former term can be estimated from the electrical conductivity by Wiedemann-Franz law with Lorentz number L:

$$\kappa_e = LT\sigma \tag{2.7}$$

Lattice thermal conductivity cannot be measured directly, but rather obtained by subtracting the electronic contribution from the total thermal conductivity. From the basic kinetics theory, the lattice thermal conductivity is expressed as:[19]

$$\kappa_l = \frac{1}{3} C_{ph} \cdot v_g \cdot l \tag{2.8}$$

where C_{ph} is the heat capacity per volume, v_g is the group velocity and l refers to the phonon mean free path. To lower the lattice thermal conductivity, one can enhance the phonon scattering and reduce the phonon mean free path, by introducing defects such as dislocations, nanoparticles/nanoinclusions.[20] Alternatively, semiconductor materials with large anharmonicity and intrinsically low lattice thermal conductivity, are good candidates for thermoelectric applications.[13]

2.3 Improving thermoelectric performance

In order to improve the thermoelectric performance, according to Equation 2.2, one needs to increase the Seebeck coefficient and electrical conductivity, meanwhile reduce the thermal conductivity as much as possible. However, from a fundamental materials perspective, it is a conflict to simultaneously improve

all three parameters; enhancing one parameter without degrading one or both of the other two would already be a significant breakthrough. For instance, doping is usually employed to improve the electrical conductivity by increasing the carrier concentration, but a high carrier concentration is unfavorable for the Seebeck coefficient, and the increase of the electrical conductivity inevitably leads to a higher electronic thermal conductivity. Nanotechnology has boosted the thermoelectric performance over the past few decades, by reducing the lattice thermal conductivity through the introduction of nanoparticles, nanoinclusions and defects. Nevertheless, without the fundamental understanding and appropriate selection of the dopants, these defects could also worsen the electrical transport properties.
Therefore, to improve these three macroscopic measurable parameters (S, σ, κ), the understanding of the microscopic structure and electron/phonon transport mechanism is needed. Herein, we summarize the strategies that are used to improve the thermoelectric performance in this thesis.

2.3.1 The phonon-glass electron-crystal (PGEC) concept

Lattice thermal conductivity is the only parameter that is independent of the carrier concentration, accordingly, tuning the lattice thermal conductivity should not affect the electrical transport properties (σ, S, κ_e). Nanostructuring could enhance phonon scattering by introducing defects and thus reduce the lattice thermal conductivity, but these defects could also scatter the electrons (holes in p-type materials) and lower the carrier mobility. Thus, finding materials with intrinsic low lattice thermal conductivity is more effective. Based on this, phonon-glass electron-crystal (PGEC) concept was proposed,[15] suggesting that materials with low lattice thermal conductivity (glass-like thermal conductivity) and high electrical conductivity (crystal-like electrical conductivity) are good candidates for thermoelectric application.
In general, glasses and amorphous materials, having no periodic arrangement of atoms, show the lowest thermal conductivity. On the other hand, crystalline materials with well-defined structure, usually exhibit excellent electrical conductivity. Following the PGEC concept, the first achievement was for skutterudite and clathrate compounds.[21, 22] They are crystalline materials containing cage-like framework structure, where guest atoms are encapsulated. Because the radius of the guest atoms is much smaller than the cage size, these guest atoms are loosely bonded and vibrate with large amplitudes.[23] As a result, the guest atoms scatter the phonon, leading to a glass-like lattice thermal conductivity. Meanwhile, electrons are conducted via bonding between the atoms of the host framework, the carrier mobility remains large enough to achieve good electrical conductivity.[24]
Recently, PGEC concept is also achieved in bulk materials beyond classic

cage structure. These materials either possess multiple structural disorder (Zn_4Sb_3),[25] large complex unit cell with rattling atoms (KMg_4Sb_3) or strong anharmonicity (SnSe).[26–28]

2.3.2 Band structure engineering

Band structure engineering usually refers to the positioning of the Fermi level in the band gap, either close or away from the conduction band minima in n-type materials (or valence band maxima in p-type materials).[29, 30] Consequently, carrier concentration is tuned, thus affecting the electrical transport properties. As is shown in Equation 2.4 and Equation 2.5, electrical conductivity and Seebeck coefficient have an opposing dependence on the charge carrier concentration, so a compromise usually exists between excellent electrical conductivity and large Seebeck coefficient in thermoelectric materials.
As a result of band structure engineering, an optimal carrier concentration is obtained and the power factor ($PF = S^2 \cdot \sigma$) is maximized, as illustrated in Figure 2.2. The peak of zT typically occurs at the carrier concentration between 10^{19} and 10^{20} cm^{-3}, which is found in heavily doped semiconductors.[3]

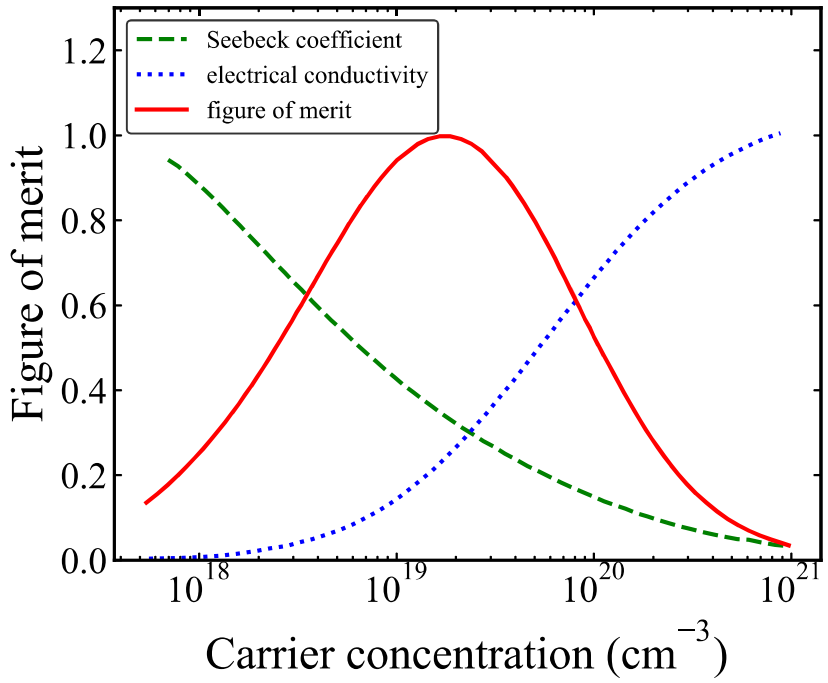

Figure 2.2: *Optimization of zT by tuning of the carrier concentration achievable through band structure engineering.*

2.3.3 Modulation doping

Modulation doping is a well-developed technique in thin-film device to increase the electrical conductivity.[31, 32] Zebarjadi et al. were among the first to employ modulation doping in SiGe alloys,[33, 34] and afterwards this method was expanded into different systems, such as BiAgSeS, BiCuSeO, PbTe and $SrTiO_3$.[35–40]
The electrical conductivity of semiconductor materials can be increased by doping, mainly through the increased carrier concentration. However, it is usually counteracted by a decrease of the carrier mobility, because the dopants could also scatter the charge carrier (ionized impurity scattering). Nevertheless, modulation doping overcomes this compromise by creating a heterostructure: an undoped matrix phase and a doped phase. Charge carriers could separate from the latter and transfer to the former, and because of the absence of the ionized impurity scattering, these charge carriers move faster in the undoped matrix. As a result, the electrical conductivity can be enhanced without decreasing the Seebeck coefficient.

2.4 Inorganic clathrates

2.4.1 Host-guest cage structure

Inorganic clathrates are covalently bonded semiconductors with relatively small band gaps and typically comprise elements from groups 13, 14 and 15 of the periodic table.[14] They have the distinctive structural motifs of three-dimensional host frameworks, which contain a variety of polyhedral cages, where guest atoms, ions and molecules are encapsulated. Clathrates are classified according to the symmetry, which determines the size and structure of the cages. With respect to the thermoelectric applications the widely investigated clathrates are of type-I. This includes the materials of interest in the thesis, which focuses on clathrates with the general formula $Z_8A_{16}B_{30}$, where Z refers to the guest atoms, A and B are the host atoms.
The crystal structure of type-I clathrate is shown in Figure 2.3, with the space group Pm-3n (International Tables of Crystallography number 223). Host atoms are located at the Wyckoff sites 6c, 16i and 24k and connected with covalent bonds, forming two different types of cages - small pentagonal dodecahedral and large tetrakaidecahedral cages. Guest atoms are encapsulated and positioned at the center of the cages, with Wyckoff positions 2a and 6d, respectively.
The type-I clathrate is known for the intrinsically low thermal conductivity.[13, 41, 42] It exhibits a crystalline structure, but the lattice thermal conductivity is close to the amorphous limit. The origin of the low thermal conductivity has been debated, but mainly attributed to the interaction between the guest

atoms and the cage-like structure.[13, 43–46] The guest atoms at the 6d site are encapsulated inside the oversized cage and loosely bonded, and thus exhibit large anisotropic atomic displacement parameter, and scatter phonons. However, the actual mechanism that induces the glass-like lattice thermal conductivity is complex, strong anharmonicity is also observed in the type-I clathrates. Therefore, the complex host-guest structure makes clathrates not only interesting for the thermoelectric application, but also for exploring the origin of the glass-like thermal conductivity.

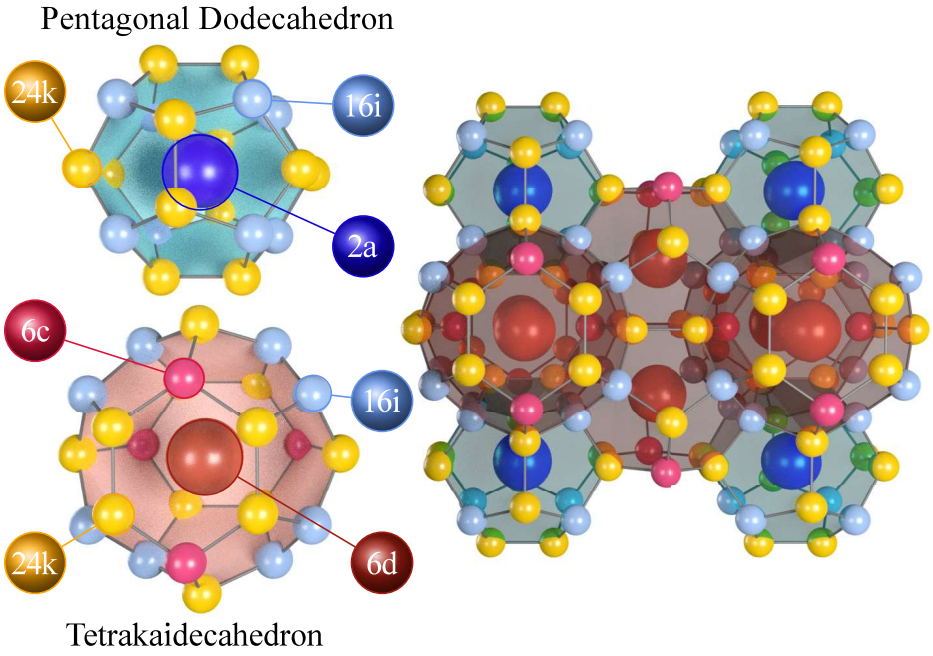

Figure 2.3: *Crystal structure of type-I clathrate (space group Pm-3n). The host atoms share Wyckoff sites 6c, 16i and 24k, forming small pentagonal dodecahedral and large tetrakaidecahedral cages, where the guest atoms are encapsulated at the center of the cages, occupying 2a and 6d sites.*

2.4.2 Zintl concept

Type-I clathrate is characterized as Zintl phase,[11] which means the guest atoms do not participate in bonding directly, but rather donate the valence electrons to the bonding among host atoms. In a typical type-I clathrate compound, $Ba_8Ga_{16}Ge_{30}$, the total number of electrons donated by the Ba atoms (nominally +2) is balanced by that of Ga (nominally -1) in a unit cell. Thus, the material should exhibit an intrinsic semiconductor behavior. However, in practice, the synthesized samples usually contain defects such as vacancies, or the real composition deviates from the stoichiometry. Thus, the samples display

doped n- or p-type semiconductor behavior.
One can design the chemical composition of clathrates according to the Zintl rule. In addition, since the band structure is mainly dependent on the bonding among the host elements, the electrical transport properties can be tuned by host elements engineering.[47]

3 Experimental Methods

3.1 Synthesis methods

3.1.1 Stoichiometric reaction

Stoichiometric reaction, sometimes called 'shake and bake', is the most straightforward synthesis method. Elements are mixed in a crucible according to the specific stoichiometry of the materials to be synthesized and heated in a furnace. Depending on the reaction temperature, it is categorized as solid-state reaction or melting reaction.
For the former, the sample is heated below the melting point and thus all materials are reacted in the solid state. The low diffusion rate due to the relative low temperature, as well as the limited contact area hinder the homogeneity of the final product. Thus, it is quite common to repeat the heat treatment several times, and between each time thoroughly grind the sample to achieve the homogenization.
Conversely, the melting reaction occurs above the melting point and all materials are in the liquid state. The reaction time is less compared to the solid-state reaction, though repeating the reaction is sometimes necessary as well.
Regarding the synthesis of clathrate compounds $Ba_8(Al_xGa_{1-x})_{16}Ge_{30}$ in this thesis, the reactants are reacted above the melting point. Some elements (such as barium) with high vapor pressure easily evaporate at the elevated temperature, hence, an extra amount of these elements is added to compensate for the loss during the reaction.

3.1.2 Flux growth

Single crystals can be grown by the flux method.[48] here, an additional compound apart from the reactants is added and serves as the flux. The flux has the lowest melting point among all the reactants and can be easily separated from the final product. Single crystal $Ba_8(Al_xGa_{1-x})_{16}Ge_{30}$ can be grown in a Ga flux. As is shown in Figure 3.1, the crystal size can be controlled from mm to cm long, depending on the amount of the extra Ga added to the reactants, the reaction temperature and time.

Figure 3.1: *Single crystals $Ba_8(Al_xGa_{1-x})_{16}Ge_{30}$ with well-defined facets grown by the flux method.*

3.2 Spark plasma sintering

To measure the thermoelectric properties, a bulk material with high density and certain dimension is required. Hence, as-synthesized powders need to be consolidated into pellets, and this can be achieved by spark plasma sintering (SPS).
SPS is a low voltage, direct pulsed current activated, pressure-assisted sintering and consolidation technique.[49] As illustrated in Figure 3.2, the powdered sample is squeezed between graphite punches and a graphite die before sintering. Graphite paper is usually inserted between the sample powder and graphite surroundings, to ensure excellent electrical and thermal contact. The whole setup is inside a vacuum chamber, avoiding any oxidation taking place during the sintering.
As the sintering starts, direct pulsed current goes through the setup, simultaneous with the application of a uniaxial pressure. High electric current is generated, typically from 1-10 kA, thus resulting in an efficient Joule heating, which could reach as high as 1000 °C/min.[50] Such a high heating rate makes SPS more competitive than conventional sintering techniques such as hot pressing, whose sintering time is usually several hours, while SPS can be done within minutes.
High electric current also results in local overheating at the contact points between powder particles.[51] Thus, melting occurs on the surfaces of the particles, and 'necks' are formed on the contact area between particles, which in turn favors the densification process.

3.2.1 Densification process

The densification of the sample during SPS is divided into three periods,[52] as described in Figure 3.3. The first period is when the temperature is below the sintering temperature. Powdered sample mainly goes through the elastic deformation under the uniaxial pressure, at the same time air is squeezed out of

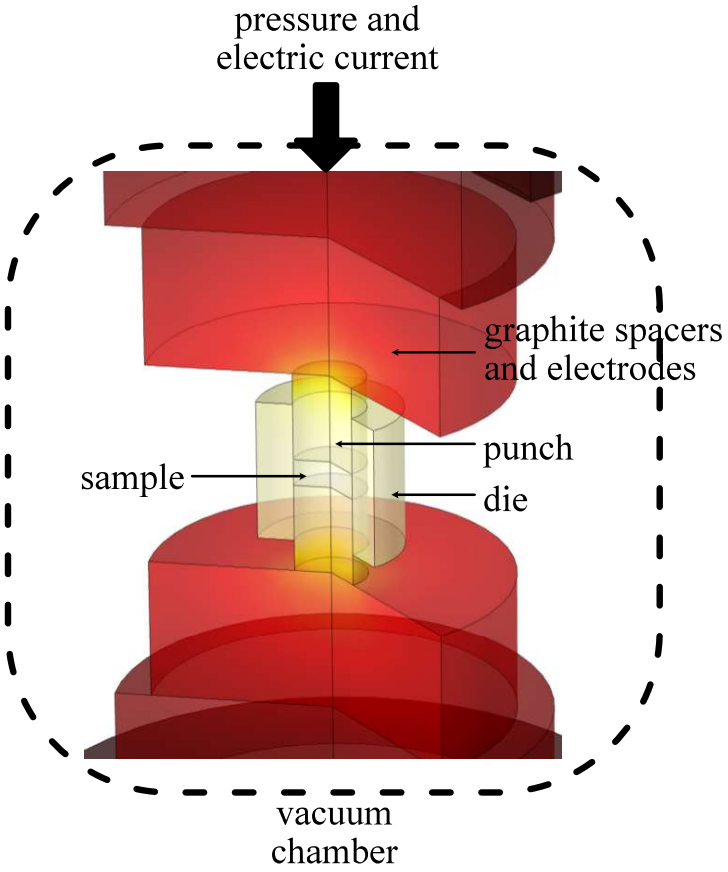

Figure 3.2: *Schematic of SPS setup.*

the sample. Temperature does not play an important role at this stage, meanwhile the density of the sample increases slightly and slowly.
The second period is when the temperature reaches the sintering temperature. The sample undergoes a rapid densification within several minutes, and sample is almost fully dense after this stage. Different densification mechanisms are suggested for this period,[50] such as vaporization-condensation, plastic deformation, surface-, grain boundary-, and volume-diffusion, but the exact nature is still unclear.
As the temperature reaches the holding temperature, the density of the sample seemingly does not increase any more, because the displacement of the punch does not change obviously (from which the density of the sample is calculated). Nevertheless, this stage is critical to fabricate homogeneous bulk materials. The temperature distribution is not homogeneous within the sample. When the temperature reaches the holding temperature, some part of the material is fully dense, but some part may still not be. Even though the material exhibits shiny metallic color on the surface, the density can vary in the interior, thus the thermoelectric properties are not homogeneous. To prevent this, an extended holding time can be favorable for homogenizing the bulk material.

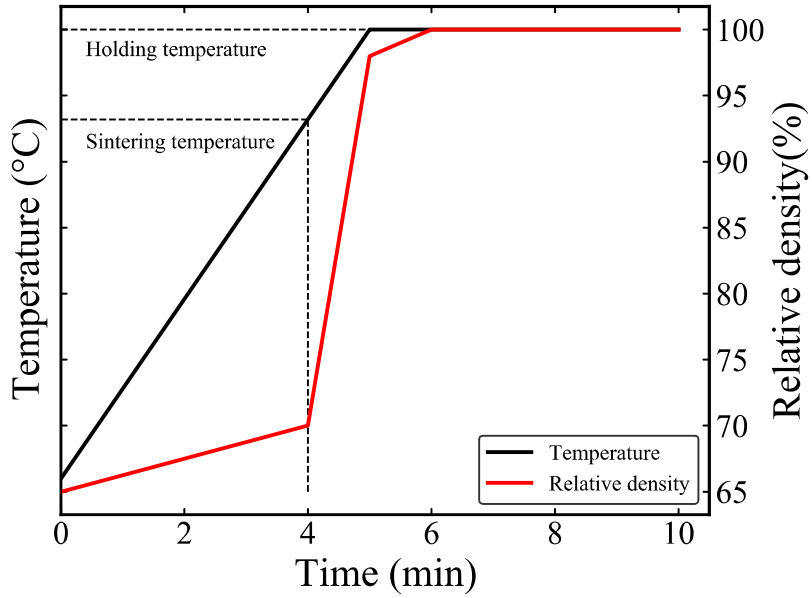

Figure 3.3: *Densification process in SPS. The temperature is measured by the thermocouple, while the density is calculated from the displacement of the punches.*

3.2.2 Simulation tools

Due to the complexity of the thermal, electrical and mechanical processes involved in the SPS, it is always a trial and error process to figure out the optimal sintering parameters. With the help of simulation tools, this procedure can be performed in a more efficient way.[49] Especially, simulation tools have proven their advantage in certain applications, for instance the temperature prediction and scaling up the production.

Finite element method is used to simulate the SPS process in my master thesis *Simulation model for the synthesis of thermoelectric materials by spark plasma sintering*. An electrical-thermal-mechanical fully coupled model was developed, which successfully predicts the densification process during the first period. However, the predicted density starts to deviate from the experimental data when the temperature reaches the sintering temperature, as illustrated in Figure 3.4. The underestimation is mainly attributed to the unclear sintering mechanism at the second period.

Even though, it is practically useful to predict the temperature distribution within the sample. A simulated temperature distribution is shown in Figure 3.5, when an Fe pellet (20 mm in diameter and 3 mm in thickness) is at the final period during SPS. It indicates that there can be a large thermal gradient within the sample, additionally, the actual temperature in the sample can be much higher than that measured by the thermocouple.

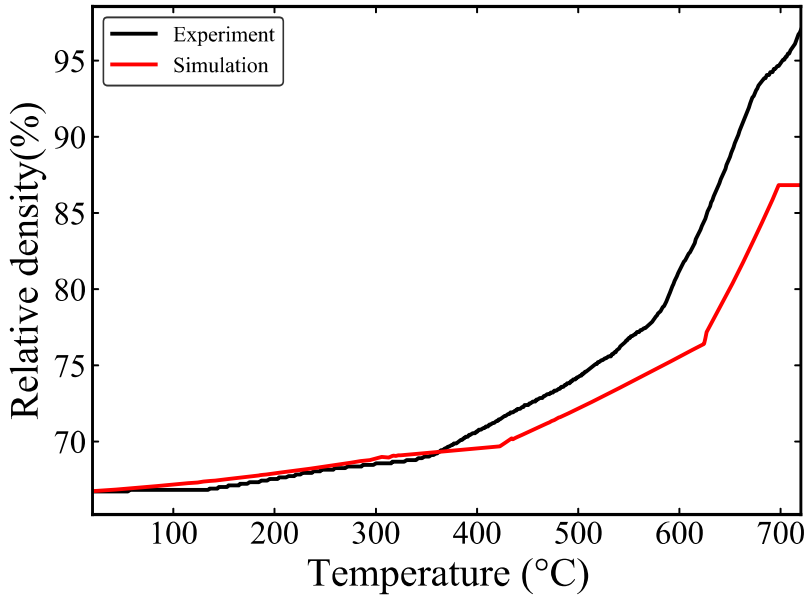

Figure 3.4: *Comparison between the experimental measured and the simulation predicted density.*

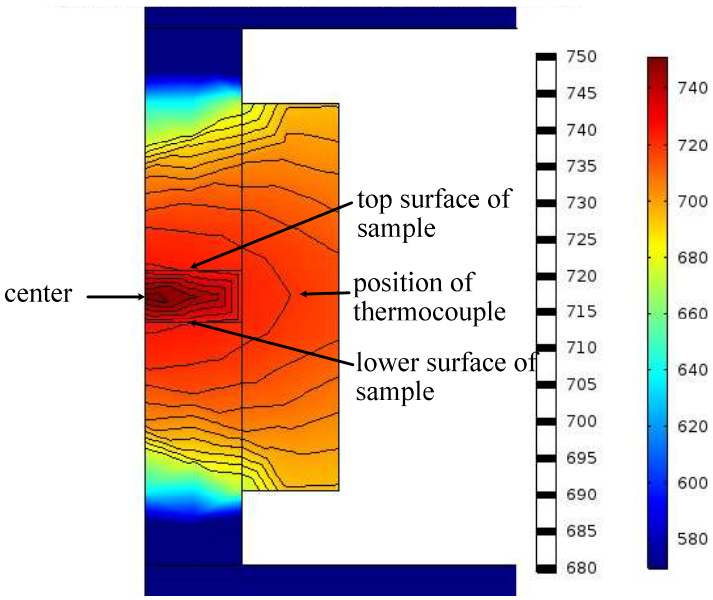

Figure 3.5: *Simulated temperature distribution within the sample during SPS, contours refer to the isothermal lines.*

In the actual SPS experiment, the temperature of the sample is probably hundreds of degrees higher than the measured temperature. Here are two examples to illustrate the problem of not knowing the actual temperature.
Fe powder was sintered under a constant heating rate and pressure, the effect of

the holding temperature is investigated. It was found that all samples reached 100 % density at the holding temperature varying from 600 - 900 °C, but the sample seemed not sintered at 400 °C because loose powder was observed on the surface. However, as the sample was sliced it was revealed that the center of the pellet was dense and showed typical metallic color, which indicates that the actual temperature during the sintering at the sample center was much higher than 400 °C.

The second case is the sintering of $Ba_8(Al_xGa_{1-x})_{16}Ge_{30}$, where metallic beads were found to leak out and remain on the graphite die. Initially these beads were thought to be Ga, which could probably melt during SPS. However, X-ray diffraction confirmed that these beads were composed of clathrate compound and Ge. Considering that the melting points of Ge and clathrate compound are higher than 900 °C while the holding temperature was only 720 °C, overheating must occur during SPS. The problem was further solved by isolating the sample by coating the graphite surroundings with boron nitride spray. As suggested from the simulation model, sample is heated in a different way when isolated: without isolation, electric current goes through the sample directly, thus Joule heating occurs within the sample and heat transfers from the sample to the surroundings; once the sample is isolated, heat transfers in the opposite direction, from the surroundings to the sample, so the temperature within the sample is always lower than the measured temperature. Additionally, isolating the sample also prevent the electric current, so the sample is not overheated.

4 Analytical Techniques

4.1 Structural characterization

4.1.1 Scanning electron microscopy (SEM)

Scanning electron microscopy SEM is a non-destructive microscopy technique, which produces images of a sample by scanning the surface with a focused beam of electrons. Sample surface is bombarded with high-energy electrons, which interact with atoms and lead to the emission of secondary electrons and backscattered electrons. Secondary electrons are ejected from conduction or valence bands of the specimen atoms by inelastic scatterings with beam electrons, providing information about the surface topography. Backscattered electrons consist of high-energy electrons originating from the electron beam which are reflected or backscattered from the specimen, and give information about surface composition.

4.1.2 X-ray fluorescence (XRF)

When materials are exposed to high-energy X-rays, electrons from the inner orbitals of their atoms are excited, leaving a 'hole' in the inner orbitals. The electronic structure of such atoms is unstable, thus electrons from the higher orbitals 'fall' into the inner and fill in the hole. Meanwhile energy is released in the form of X-rays, which is equal to the energy difference between the two orbitals involved. This phenomenon is called X-ray fluorescence. Each element has its own characteristic X-ray emission spectrum. By detecting the spectrum, the composition of the specimen can be quantified.
X-ray fluorescence analysis (XRF) consists of two methods, energy-dispersive (EDX) and wavelength-dispersive X-ray spectroscopy (WDX). The former is implemented in SEM, allowing a quick and semi-quantitative analysis of the composition. Opposite to EDX which measures the X-ray in the whole energy spectrum, WDX measures the emitted X-ray of a single wavelength. Therefore, WDX provides higher spectral resolution so that it can distinguish the elements whose characteristic X-ray peaks are too close to be resolved by EDX. In addition, WDX has lower detection limits ($<$ 100 - 500 ppm) than EDX (1000 - 5000 ppm).

4.1.3 X-ray diffraction (XRD)

The X-ray diffraction (XRD) technique is widely used for studies of inorganic materials, for the purpose of phase identification, crystal structure determination and strain and texture analysis. In this thesis, different diffraction techniques are performed in order to determine the atomic structure of the clathrate compounds, including neutron and X-ray diffraction, on samples in the form of both powders and single crystals.
A crystal is defined as a periodic arrangement of atoms or molecules. When a crystal is bombarded with X-ray beams, as is illustrated in Figure 4.1, only those incident beams that satisfy certain criteria would be diffracted and observed at certain directions. This rule is called Bragg's law:

$$2d_{hkl} \cdot sin\theta = n\lambda \tag{4.1}$$

Here, n is any integer and λ is the wavelength of the X-ray beam. Accordingly, by measuring all the observable diffraction angles, and correspondingly the interplane distances d_{hkl}, the space group of the crystal can be determined.

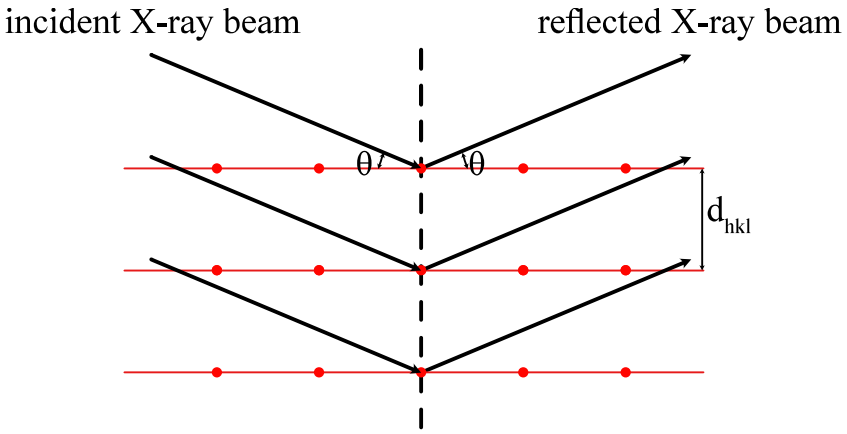

Figure 4.1: *Illustration of X-ray diffraction. Here red dots refer to the periodic arrangement of atoms, and red lines are the atomic planes with Miller indices (hkl) and interplane distance d_{hkl}. θ is the angle between the incident X-ray beam and the atomic plane.*

However, at this point, the crystal structure is not solved yet, as the elements on those positions are still unknown. To determine this, the intensity of each reflection needs to be analyzed. The intensity of each reflection (I_{hkl}) is proportional to the square of the so-called structure factor (F_{hkl}), which is defined by:

$$F_{hkl} = osf \cdot \sum_{j=1}^{N} f_j \cdot e^{2\pi \cdot (hx_j + ky_j + lz_j)} \cdot T_j \cdot occ_j \tag{4.2}$$

Here, *osf* refers to the overall scale factor, f_j is the atomic form factor, x_j, y_j, z_j indicate the position of the atom, T_j and occ_j denote the temperature factor and site occupancy factor of the atom, respectively. Thus, knowing the structure factor, the atomic position, atomic displacement parameter and site occpuation can be determined.
Instead of calculating the structure factor directly from the intensity of the reflections, the crystal structure is solved and refined in the opposite way: creating a crystal structure and calculating the corresponding structure factor and intensity of each reflection, comparing the calculated values with the experimentally observed ones and minimizing the difference via least squares method. When reasonable goodness-of-fitness parameters are achieved, the simulated crystal structure is suitable to describe the actual atomic structure of the crystal.
The crystal structure solution is a comprehensive problem, here only the general principles are briefly mentioned. Next, the difference between different diffraction techniques will be discussed, and why these experiments are performed in this thesis.
Single crystal diffraction is conventionally used for solving the crystal structure, while powder diffraction is more commonly used in structure refinement, which means the space group is already known but additional information needs to be refined, such as the grain size and shape, or the strain and texture. The main difference is that powder diffraction merges all the symmetry-equivalent reflections to a peak, so the observable reflections in powder diffraction are not adequate to determine the space group. In **Paper II**, the crystal structure of $Ba_8(Al_xGa_{1-x})_{16}Ge_{30}$ is determined by single crystal diffraction. Although the crystal structure of clathrate compounds $Ba_8Al_{16}Ge_{30}$ and $Ba_8Ga_{16}Ge_{30}$ is already examined, it is still necessary to use single crystal diffraction to check the possible existence of a superstructure in the quaternary compounds $Ba_8(Al_xGa_{1-x})_{16}Ge_{30}$.
Both X-rays and neutrons can be utilized to characterize the crystal structure. A fundamental difference is that X-rays interact with the electron density of an atom, so it can tell information about the chemical bonding, while neutrons interact with the nuclear density and therefore provides more precise information about the atoms. In addition, the scattering cross section (or scattering length) shows different elemental dependence. X-ray diffraction is not able to distinguish neighboring elements in the period table, because they exhibit similar scattering cross section, while neutron diffraction has a very complex elemental and isotope scattering length dependence. In **Paper II**, we utilize this characteristic and study the crystal structure of quaternary clathrate compound $Ba_8(Al_xGa_{1-x})_{16}Ge_{30}$, to solve the site occupation of Al, Ga and Ge in the host framework.

4.2 Characterization of thermoelectric properties

4.2.1 Electrical resistivity and Seebeck coefficient

The electrical resistivity (ρ) and Seebeck coefficient (S) are simultaneously measured by the ZEM3 instrument (Ulvac). The sample is fixed by two electrodes from the top and bottom sides, respectively, and attached to two probes on the side. In order to protect the electrodes and probes, graphite paper is inserted between them and the sample. The measurement is conducted in a low-pressure helium atmosphere.
As illustrated in Figure 4.2, when measuring the resistivity of the specimen, a constant current is sent through the sample, meanwhile the voltages are measured by two probes. The resistance of the sample can be calculated by dividing the potential difference by the constant current. With the known cross-sectional area of the specimen and the distance between two probes, the resistivity of the specimen can be determined.
The Seebeck coefficient is measured by creating a thermal gradient along the sample by heating the sample from the bottom electrode. The probes are able to measure the voltage and temperature simultaneously. The measured voltage is composed of both the actual Seebeck voltage and noise. In order to improve the accuracy, the measurement at each temperature is repeated by creating different thermal gradients along the sample, and the Seebeck coefficient is calculated according to Equation 2.3.

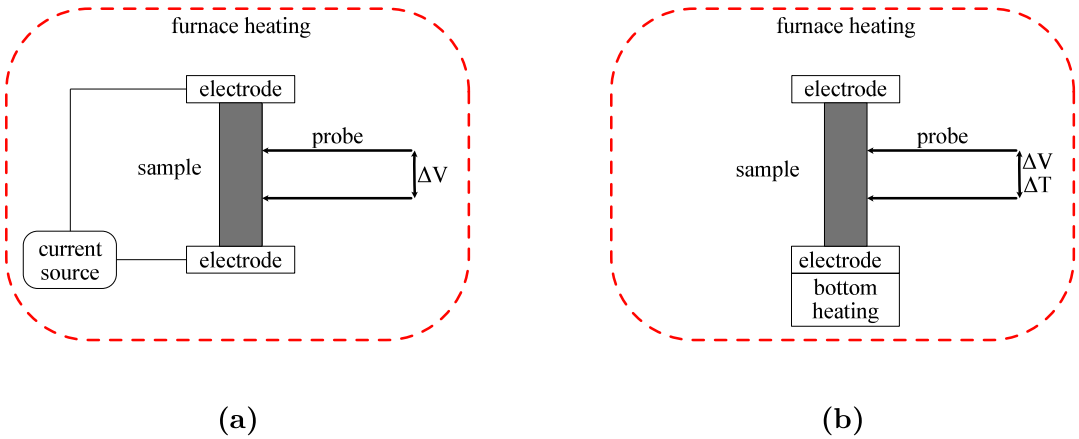

Figure 4.2: *Schematic of ZEM3 instrument for the measurements of (a) electrical resistivity, (b) Seebeck coefficient.*

4.2.2 Thermal conductivity

The thermal conductivity of the materials is measured using the transient plane source technique (TPS) implemented in the instrument Hot Disk TPS 3500.[53] Hot Disk sensors are composed of an electrically conducting film in the shape of a double spiral which is made of nickel, and two sheets of electrically insulating materials sandwiching the nickel film. These insulating materials are used for supporting the film at high temperature and also preventing the reaction between the sensor and the measured specimen. When performing the measurement, the sensor is tightly sandwiched between two identical samples in a furnace with helium atmosphere.
The TPS sensor serves as both a heater and a temperature sensor. Heat is generated by Joule heating in the sensor by sending an electric current through it. The temperature is obtained by measuring the resistance of the sensor using a four-probe setup and converting the resistance to temperature by the known temperature coefficient of resistivity (TCR) of nickel. During the measurement, a precise amount of heat is generated in the sensor, the recorded resistance of the sensor can be expressed as:

$$R(t) = R_0 \cdot \left[1 + \alpha \cdot \triangle T_i + \alpha \overline{\triangle T(\tau)}\right] \tag{4.3}$$

Here, R_0 is the resistance of the TPS sensor before the measurement and α is the TCR. $\triangle T_i$ refers to the temperature difference between sensor and the thin insulating layer, which becomes constant after a very short time. $\overline{\triangle T(\tau)}$ is the time dependent temperature increase of the sample surface. The expression can be rewritten as:

$$\overline{\triangle T(\tau)} + \triangle T_i = \frac{1}{\alpha}\left[\frac{R(\tau)}{R_0} - 1\right] \tag{4.4}$$

Meanwhile, the theoretical temperature increase of the sample surface is given by:

$$\overline{\triangle T(\tau)} = \frac{P_0}{\pi^{1.5} \cdot r \cdot \kappa} D(\tau) \tag{4.5}$$

where P_0 and r denote the heating power and radius of the sensor, respectively. κ is the thermal conductivity of the tested sample and $D(\tau)$ is a dimensionless time-dependent function which includes the thermal diffusivity and specific heat capacity of the tested sample. Therefore, the plot of $D(\tau)$ against $\overline{\triangle T(\tau)}$ should be a straight line, from which the slope of the straight line can be calculated, and the thermal conductivity of the sample is obtained.

4.2.3 Specific heat capacity

The specific heat capacity (C_p) of the materials was measured with a differential scanning calorimetry instrument (Mettler Toledo) and the sapphire method

(E1269 - 11). To determine C_p, Measurements were performed on the heat flow of the empty crucible, the crucible with the specimen and the crucible with a sapphire standard. C_p of the specimen is calculated by:

$$C_p = \frac{H_{sample} - H_{crucible}}{m_{sample}} \cdot \frac{m_{sapphire}}{H_{sapphire} - H_{crucible}} \cdot C_p(sapphire) \tag{4.6}$$

here, H refers to the heat flow for each measurement and m is the mass.
To obtain a reasonable result, a criterion is that the heat capacity of the measured sample ($C_p \cdot m$) should be close to that of the sapphire standard. Another criterion is the selection of the crucible, which should be composed of highly thermal conductive materials, such as aluminum, platinum or gold. The size of the crucible should satisfy the rule that three quarters are full of the tested sample, so that the heat can conduct to the sample efficiently.

5 Results and Discussion

The motivation of this thesis, is to achieve a deeper understanding of the effect of structure on the electron and phonon transport mechanisms, as well as to optimize the thermoelectric properties of inorganic clathrates in an experimentally controllable way.
In **Paper I** we explored the modulation doping in $Ba_8(Al_xGa_{1-x})_{16}Ge_{30}$ and studied the impact of microstructure on the thermoelectric properties. Here, polycrystalline samples of $Ba_8(Al_xGa_{1-x})_{16}Ge_{30}$ were synthesized through ball milling and spark plasma sintering of mixtures of $Ba_8Al_{16}Ge_{30}$ and $Ba_8Ga_{16}Ge_{30}$. While in **Paper II**, single crystals of $Ba_8(Al_xGa_{1-x})_{16}Ge_{30}$ were synthesized and the structure was investigated by a combination of X-ray and neutron diffraction. The obtained crystal structure, especially the chemical ordering in host sites, is validated by theoretical calculations. Furthermore, the impact of synthesis methods on the atomic structure is illustrated.

5.1 Polycrystalline $Ba_8(Al_xGa_{1-x})_{16}Ge_{30}$ synthesized by ball milling and spark plasma sintering

5.1.1 Electrical transport properties

Polycrystalline $Ba_8(Al_xGa_{1-x})_{16}Ge_{30}$ (x = 0, 0.20, 0.23, 0.25, 0.33, 0.50 and 1) were synthesized via ball milling and spark plasma sintering of mixtures of $Ba_8Al_{16}Ge_{30}$ and $Ba_8Ga_{16}Ge_{30}$. The electrical transport properties are shown in Figure 5.1a and 5.1b. All samples have negative Seebeck coefficient and thus demonstrate an n-type semiconductor behavior. The high absolute Seebeck coefficient and resistivity indicates that the $Ba_8Ga_{16}Ge_{30}$ material is only slightly doped and has a relatively low carrier concentration. On the other hand, $Ba_8Al_{16}Ge_{30}$ exhibits the lowest resistivity and absolute Seebeck coefficient, meaning the compound is heavily doped thus possesses high carrier concentration. According to the band structure engineering, the carrier concentration can be tuned by alloying $Ba_8Al_{16}Ge_{30}$ with $Ba_8Ga_{16}Ge_{30}$, and this is observed herein: the gradually increased amount of $Ba_8Al_{16}Ge_{30}$, gradually decreases the resistivity and the absolute value of the Seebeck coefficient.
By tuning the doping level slightly ($0.20 \leq x \leq 0.25$), the resistivity can be further decreased, achieving approximately 30 % reduction in the whole temperature

range from 100 - 700 °C. On the other hand, the reduction of absolute Seebeck coefficient is not that large, decreasing only slightly from -161 $\mu V^{-1}K^{-1}$ (x = 0.20) to -154 $\mu V^{-1}K^{-1}$ (x = 0.25) at 700 °C. More intriguingly, compared to the single crystal $Ba_8(Al_{0.25}Ga_{0.75})_{16}Ge_{30}$, the sintered sample x = 0.25 shows similar Seebeck coefficient but a lower resistivity in the entire temperature range studied, as is shown in Figure 5.1c and 5.1d. The similar values of the Seebeck coefficient indicate that the carrier mobility of the sintered samples is not lower than that of the single crystal. Therefore, the improved resistivity and nearly unchanged Seebeck coefficient strongly supports the idea that the sintered samples (x = 0.23 and 0.25) are modulation doped.

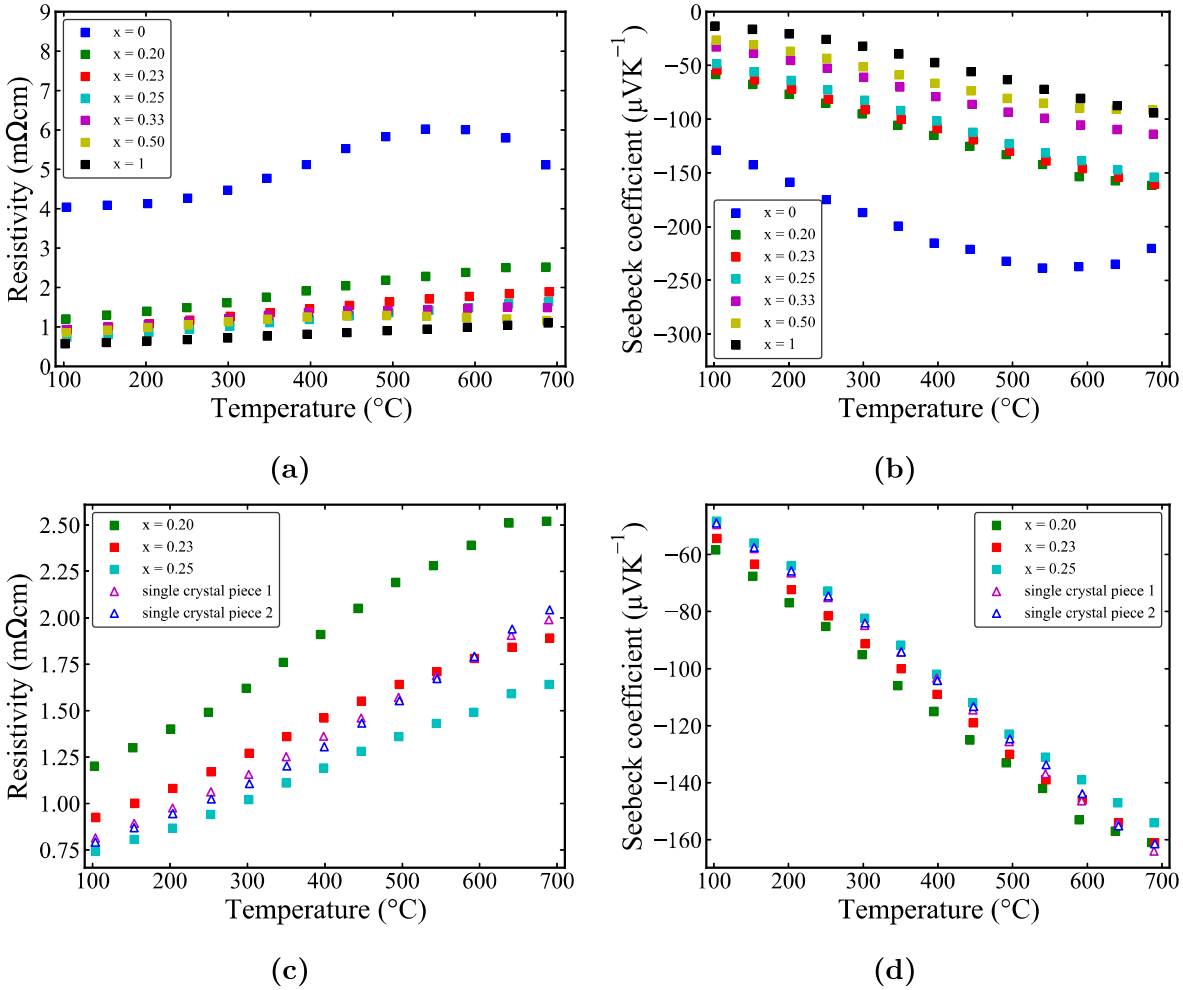

Figure 5.1: *(a, c) Electrical resistivity and (b, d) Seebeck coefficient of* $Ba_8(Al_xGa_{1-x})_{16}Ge_{30}$ *materials pressed into pellets by SPS, which in (c) and (d) are compared to the properties of two sections from a Czochralski-grown* $Ba_8(Al_{0.25}Ga_{0.75})_{16}Ge_{30}$ *single crystal.*

In order to further illustrate the origin of the improved transport properties, the

charge carrier mobility needs to be examined in more depth. As is shown in Figure 5.2, alloying $Ba_8Ga_{16}Ge_{30}$ with $Ba_8Al_{16}Ge_{30}$ reduces the carrier mobility, but noticeably, the mobility of samples x = 0.23 and 0.25 is significantly higher than that of other sintered samples. More astonishingly, the mobility of these two samples (x = 0.23 and 0.25) is comparable and even higher than that of the single crystal. The carrier mobility of the sintered sample should normally be decreased compared to the single crystal, due to the presence of grain boundaries. However, it is not observed here. Therefore, we can attribute the greatly enhanced carrier mobility in our sintered samples (x = 0.23 and 0.25) to modulation doping. In turn, this leads to a lower electrical resistivity while the Seebeck coefficient remains unchanged.

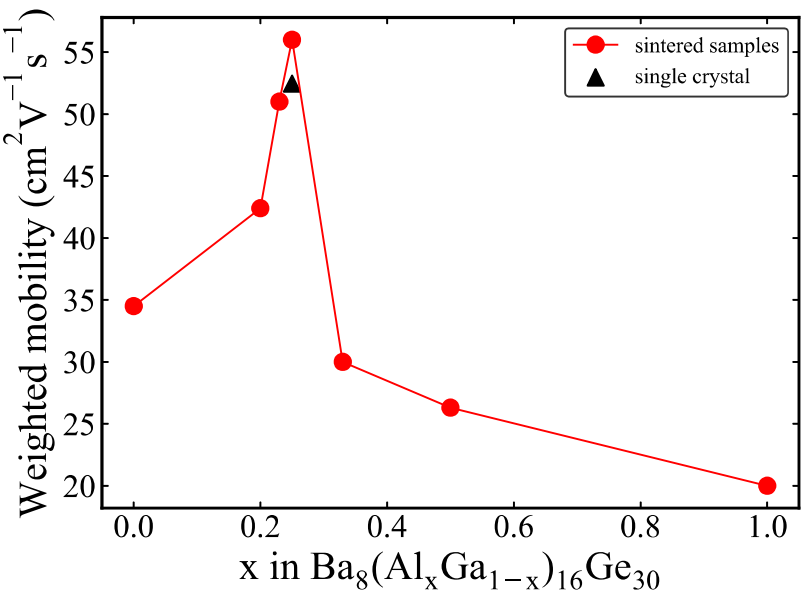

Figure 5.2: *Weighted carrier mobility for $Ba_8(Al_xGa_{1-x})_{16}Ge_{30}$ for the SPS sintered samples and the single crystal.*

5.1.2 Microstructure

The microstructure of sample x = 0.25 was studied using electron microscopy, as shown in Figure 5.3. The areas 1 and 3 display chemical compositions around $Ba_8Al_{2.9}Ga_{11.3}Ge_{28.0}$ and $Ba_8Al_{2.8}Ga_{11.9}Ge_{27.9}$. These measured values are very close to the composition of the clathrate compound considering the measurement accuracy. Since the composition appears consistent throughout each area, there exists no evidence of any phase separation of the quaternary $Ba_8(Al_xGa_{1-x})_{16}Ge_{30}$ within the individual grains. In addition, particles, with sizes of about a few hundred nanometers, are observed inside the grains as well as

along the boundaries. Such a microstructure could potentially enhance phonon scattering, and, thus, reduce the lattice thermal conductivity.
According to the Al element map shown in Figure 5.3, those hundred-nanometer-sized particles are likely to consist mainly of Al. Some Al particles are partially oxidized, which may take place during polishing. Because the oxidization only affects the sample surface, not the whole bulk, this sample still exhibits excellent electrical conductivity. Moreover, it is evident that Al is not homogeneously distributed throughout the sintered sample, but rather appears in higher concentrations in some areas, which include aggregation at the grain boundaries and particles inside the grains. Electron transfer from the Al particles to the main, Ga-rich, clathrate phase can be achieved without reducing the mobility significantly, which leads to an improved electrical conductivity without decreasing the Seebeck coefficient.

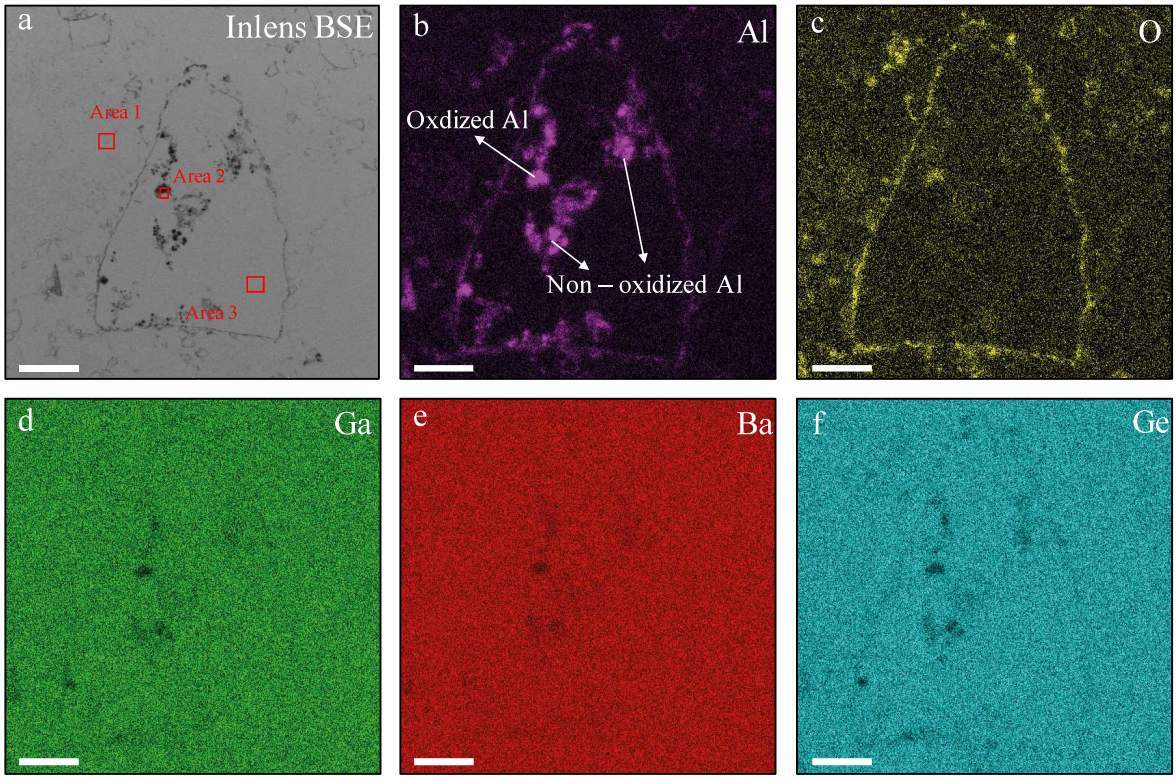

Figure 5.3: *SEM analysis of a clathrate grain in the SPS sintered sample* $Ba_8(Al_{0.25}Ga_{0.75})_{16}Ge_{30}$ *showing (a) in-lens backscattered electron (BSE) micrograph, and (b) - (f) elemental distribution maps of (b) Al, (c) O, (d) Ga, (e) Ba, and (f) Ge. The average compositions of the selected areas measured by EDX are* $Ba_8Al_{2.9}Ga_{11.3}Ge_{28.0}$ *(area 1),* $Ba_8Al_{77.2}Ga_{8.1}Ge_{23.3}O_{29.8}$ *(area 2) and* $Ba_8Al_{2.8}Ga_{11.9}Ge_{27.9}$ *(area 3), respectively. Scale bar is 10 µm.*

5.1.3 Thermal conductivity and figure of merit

The thermal conductivity of samples (x = 0, 0.20, 0.25 and 0.33) is shown in Figure 5.4a. All samples display a relatively low thermal conductivity, with the value increasing with x. The thermal conductivity tends to increase rapidly at high temperature, owing to the excitation of minority charge carriers (the bipolar effect). In order to further analyze the effect of the microstructure on the thermal conductivity, the lattice thermal conductivity is calculated and shown in Figure 5.4b. Alloying $Ba_8Ga_{16}Ge_{30}$ with $Ba_8Al_{16}Ge_{30}$ drastically reduces the lattice thermal conductivity. The minimum lattice thermal conductivity of sample x = 0.20 at 600 °C is close to the theoretical limit value for $Ba_8Ga_{16}Ge_{30}$, represented by the dashed line in Figure 5.4b. The reduction of the lattice thermal conductivity is even more pronounced for sample x = 0.25, where κ_l is extremely low and remains unchanged from 100 - 300 °C.
The significant decrease in thermal conductivity is most likely due to enhanced phonon scattering through two mechanisms: atomic-scale disorder as well as the presence of mesoscale grains with varying composition and size. The former refers to the fact that the substitution of Ga with Al induces mass fluctuation scattering in the host structure while the the latter is caused by the Al particles/inclusions, which can also scatter heat-carrying phonons.
As a result of modulation doping, the highest power factor is achieved for sample x = 0.25 with the value of 1.45 $mWm^{-1}K^{-2}$ at 700 °C, as shown in Figure 5.4c. By comparison, the power factor of $Ba_8Ga_{16}Ge_{30}$ is 0.95 $mWm^{-1}K^{-2}$ at 700 °C, so approximately 50 % improvement is achieved. The thermoelectric properties were further measured up to 800 °C, the values of zT for the $Ba_8(Al_xGa_{1-x})_{16}Ge_{30}$ materials were calculated and are shown in Figure 5.4d. The value of zT for $Ba_8Ga_{16}Ge_{30}$ reaches its maximum at 550 °C with the value of 0.69. With the introduction of $Ba_8Al_{16}Ge_{30}$, sample x = 0.20 exhibits a maximum measured zT of 0.67 at 600 - 650 °C, which decreases at higher temperature. The optimal zT is achieved for samples x = 0.23 and 0.25, with value of 0.93 and 0.99 at 800 °C.

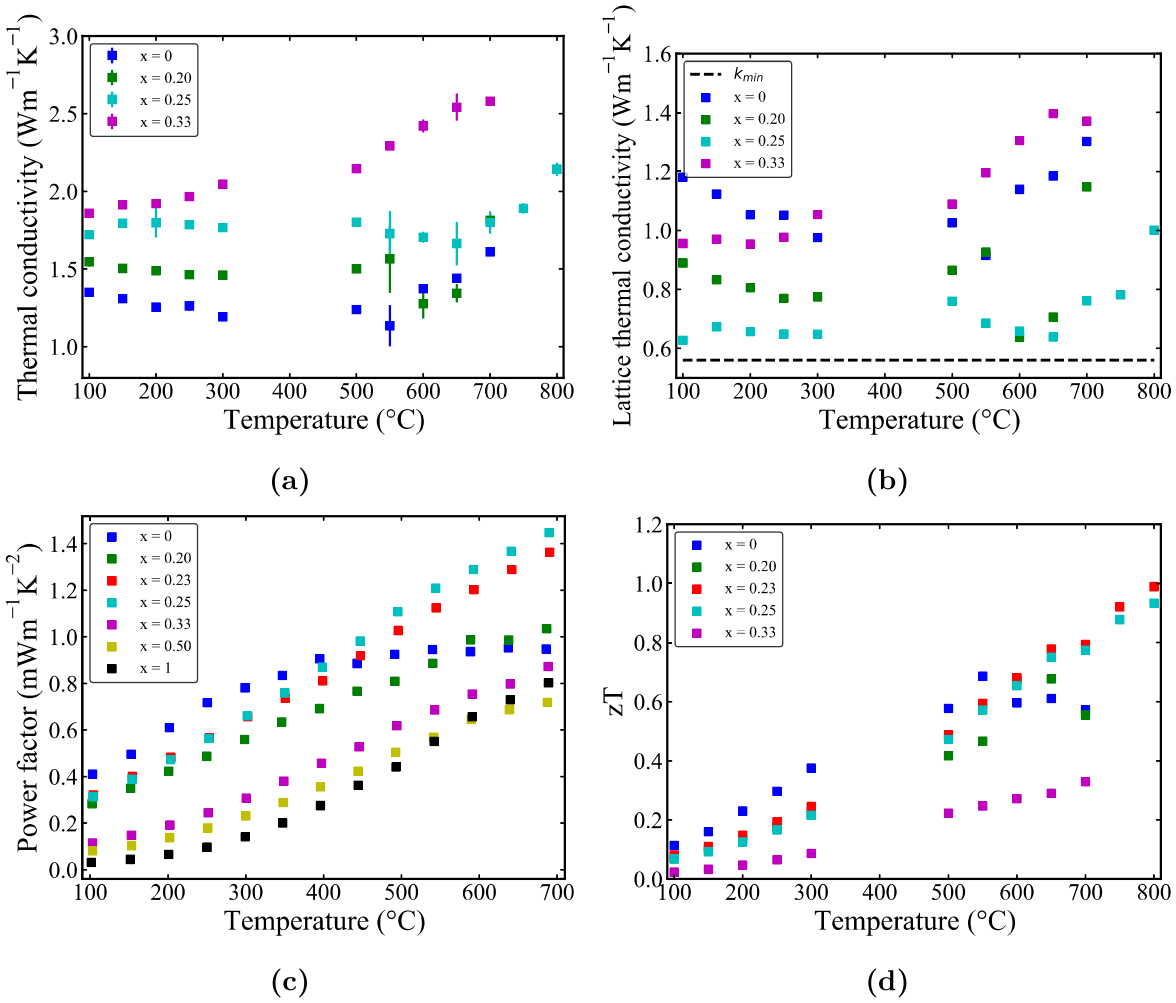

Figure 5.4: *(a) Thermal conductivity and (b) lattice thermal conductivity of* $Ba_8(Al_xGa_{1-x})_{16}Ge_{30}$*, (x = 0, 0.20, 0.25 and 0.33).* κ_{min} *refers to the theoretical minimum lattice thermal conductivity of* $Ba_8Ga_{16}Ge_{30}$*. (c) Power factor and (d) zT of* $Ba_8(Al_xGa_{1-x})_{16}Ge_{30}$ *samples.*

5.2 Single crystal $Ba_8(Al_xGa_{1-x})_{16}Ge_{30}$

5.2.1 Methodology of studying crystal structure of quaternary type-I clathrate

Recently, quaternary type-I clathrates have been widely studied, and unconventional elements are introduced into the host framework, such as transition metals or even group 15 elements.[54–57] However, the chemical ordering of those quaternary clathrates has not been well understood, probably because of the neighboring-element problem.[58] Neighboring-element problem refers to determining the composition and structure of the materials containing neighboring elements, whose characteristic peaks overlap in X-ray fluorescence

spectrum, or have similar X-ray scattering cross section. It is even more difficult for the quaternary $Ba_8(Al_xGa_{1-x})_{16}Ge_{30}$ compounds, because the material contains only 3 - 5 wt. % of the lightest element Al.

Paper II employs conventional X-ray and neutron diffraction and studies the chemical ordering in $Ba_8(Al_xGa_{1-x})_{16}Ge_{30}$, and compare the results with theoretical calculations, with the following methodology.

Samples were first measured by single crystal X-ray diffraction. Owing to the fact that the space group of both $Ba_8Ga_{16}Ge_{30}$ and $Ba_8Al_{16}Ge_{30}$ is Pm-3n, the space group of $Ba_8(Al_xGa_{1-x})_{16}Ge_{30}$ is also determined as Pm-3n. Since Ga and Ge have similar X-ray cross section, the site occupation of these two elements are not refined, but only Al is refined in the X-ray diffraction. Host atoms (Al, Ga and Ge) are sharing Wyckoff sites 6c, 16i and 24k, while guest atoms Ba are located at the center of the cages, 2a and 6d sites, respectively. All sites are assumed to be 100 % occupied with isotropic atomic displacement parameter (ADP), except for Ba at 6d sites, which possesses anisotropic ADP. The composition obtained from the structure refinement is compared with that from XRF.

Next, the chemical ordering of Ga and Ge is examined by neutron diffraction. The structure refinement is similar to the one mentioned above, but with a few restraints: the site occupancy factors (sof) of Al is not refined but fixed; the number of Ge atoms is set to 30 per unit cell. The obtained refinement results from neutron diffraction are comparable to those from X-ray diffraction, meaning that both structure refinements are reasonable, and the sample quality is high (approximately 3 g samples were measured by powder neutron diffraction). Few impurity peaks are observed in powder neutron diffraction patterns, but the intensity is low, and we did not observe these peaks in laboratory powder X-ray diffraction, so they are excluded in the refinement.

Finally, the chemical ordering determined by the experiments is compared to the results from theoretical calculations. The theoretical calculation is a combination of density functional theory, alloy cluster expansion and Wang Landau simulations, the details of which will be published in a separate study.

5.2.2 Composition of single crystals

Single crystals $Ba_8(Al_xGa_{1-x})_{16}Ge_{30}$ were synthesized by Ga-flux method, as shown in Figure 3.1, the obtained crystals have well-defined facets and the size varies from 1 - 3 mm. In addition, another single crystal was grown by Czochralski method. Here, 'C-Al5.2' refers to the sample grown by the Czochralski method, '5.2' indicates the number of Al atoms per unit cell, which is determined from the structure refinement of X-ray diffraction data, while 'F-Alxx' denotes the samples synthesized by the flux method, where 'xx' means the number of Al atoms per unit cell.

The composition of the single crystals was measured by X-ray fluorescence

analysis (XRF) and is summarized in Table 5.1. The Ge content is determined to be 29.1 - 30.5 atoms per unit cell, consistent with the stoichiometric composition.

Table 5.1: *Elemental composition of $Ba_8(Al_xGa_{1-x})_{16}Ge_{30}$ obtained from XRF and XRD*

	XRF				XRD	
Sample	Ga	Ge	Ga+Ge	Al	Ga+Ge	Al
F-Al0.0	15.4	30.0	45.4	/	45.2(3)	/
C-Al5.2	11.5	30.5	42.0	4.0	40.8(8)	5.2(8)
F-Al6.3	11.5	30.0	41.5	4.5	39.7(8)	6.3(8)
F-Al6.7	11.0	30.3	41.3	4.7	39.3(8)	6.7(8)
F-Al7.4	9.7	29.3	39.0	7.0	38.6(8)	7.4(8)
F-Al8.8	8.4	29.1	37.5	8.5	37.2(8)	8.8(8)

The lattice parameter of $Ba_8(Al_xGa_{1-x})_{16}Ge_{30}$ was obtained from single crystal X-ray diffraction data at 300 K and is shown in Figure 5.5. The increase of Al atoms substituting Ga atoms in the unit cell gradually increases the lattice parameter, consistent with the fact that $Ba_8Al_{16}Ge_{30}$ has a larger lattice parameter than $Ba_8Ga_{16}Ge_{30}$. The compositional dependence of the lattice parameter is roughly linear, probably because the host elements are not totally disordered, the Vegard's law might not perfectly apply to the clathrate system.

5.2.3 Chemical ordering in host sites

In order to study the chemical ordering of the host sites, the site occupancy factors of host elements are shown in Figure 5.6. Excellent consistency between experiment and simulation is achieved, for the single crystal grown by Czochralski method. However, the deviation for the flux-grown samples are relatively large, probably because extra Ga is added in the experimental synthesis, which could act as another driving force for the chemical ordering, while in the theoretical calculation only stoichiometric composition $Ba_8(Al_xGa_{1-x})_{16}Ge_{30}$ is considered. With the incorporation of Al, the Ge occupation at all sites remains more or less constant, meaning that only Ga is substituted by Al. This can be understood by the Zintl concept that Ge has four valence electrons, while both Al and Ga are trivalent elements, thus the substitution of Ga with Al would not change the electron balance of the material. However, the theoretical calculation predicts that Ge site occupation also changes with Al content, and the deviation from experimental data is large at the 16i and 24k sites. We suspect that theoretical calculation predicts the thermodynamically stable structure and stoichiometric

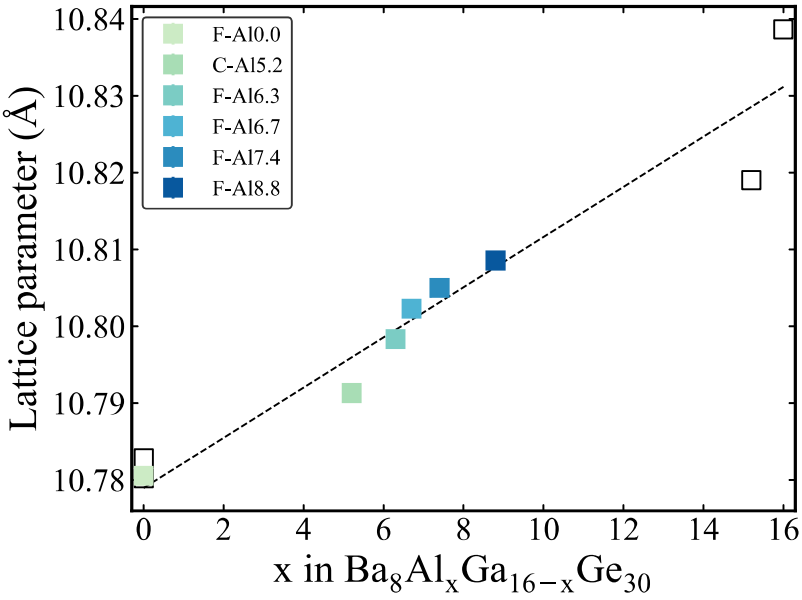

Figure 5.5: *Lattice parameter at 300 K versus Al content, where Al content (x) is calculated from the structure refinement of XRD data. The uncertainty in lattice parameter is small so the error bar is not visible. The dashed line represents a linear dependence of the lattice parameter on the Al content. Black unfilled square markers refer to the lattice parameters of* $Ba_8Ga_{16}Ge_{30}$ *and* $Ba_8Al_{16}Ge_{30}$*, with values taken from the references.*

composition, but in practice other factors are also included, such as defects and extra Ga flux.

Furthermore, Al are found on all the host sites, rather than specifically occupying certain sites. As indicated by the black dashed lines in Figure 5.6, Al is quite randomly distributed at 16i and 24k sites, which is also the case for Ga at the 24k site. Such a random distribution is observed for all the samples, despite the synthesis method. Previously, a random site occupancy factor at the 24k site was already reported for the $Ba_8Al_{16}Ge_{30}$ synthesized using an Al flux method. In the quaternary $Ba_8(Al_xGa_{1-x})_{16}Ge_{30}$ with the increase of entropy, the structure is expected to be more disordered, thus a random distribution of Al at 16i and 24k sites can be expected.

In contrast, the site occupation at the 6c site explicitly differs for the samples synthesized by different methods. The Al site occupation at the 6c site in the Czochralski sample is higher than the flux samples, while the Ga occupation shows the opposite. If following the hypothesis that the site disorder is the main factor, the site occupation at the 6c site should show the same trend, regardless of the synthesis method. But in fact, the Ga occupation at the 6c site is clearly higher for the samples grown by flux method, which is probably due to the extra Ga used during the synthesis.

To summarize, Al mainly substitutes Ga in the unit cell and does not affect Ge. The substitution takes place at all the host sites, and for the 16i and 24k sites Al shows random atomic distribution despite the synthesis methods. Conversely, the site occupation at the 6c site is highly influenced and depends on the synthesis methods.

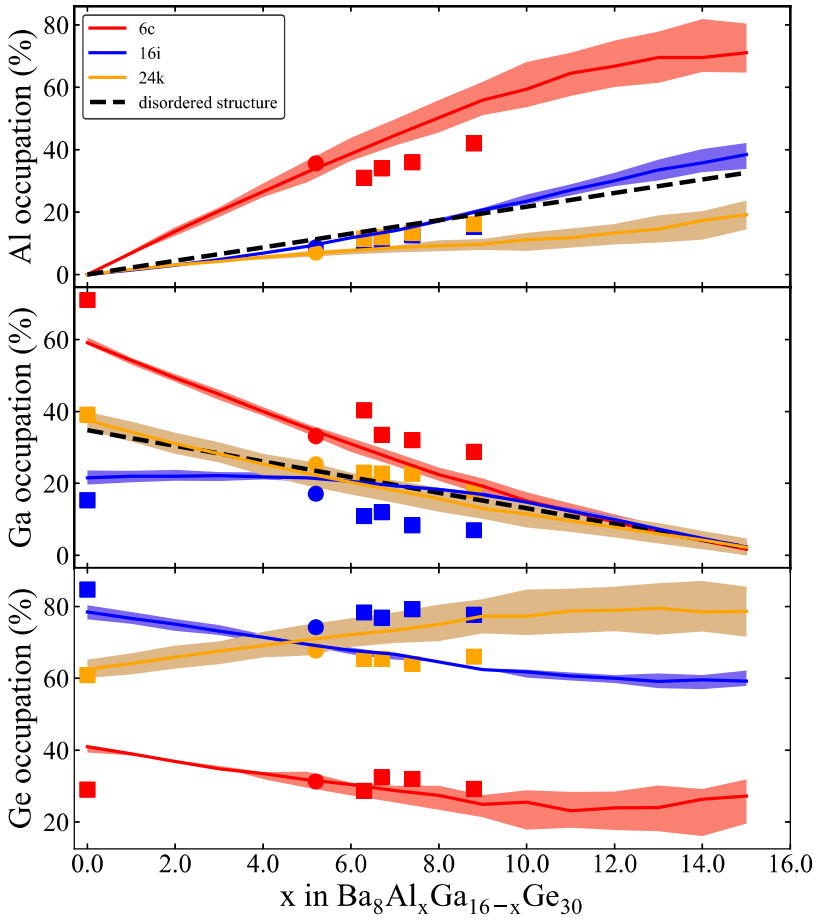

Figure 5.6: *Site occupancy factors of Al, Ga and Ge. Data points are from experimental structure refinement of X-ray and neutron diffraction data, where square markers refer to flux grown samples and circle markers denote the sample grown by Czochralski method. The solid lines are from theoretical calculations and the shaded areas represent the uncertainty of the calculations. Black dashed lines indicate the site occupation of a totally disordered structure.*

5.2.4 Atomic displacement parameters of guest atoms

The inorganic clathrate is known for its intrinsically low thermal conductivity. It exhibits a crystalline structure, but the lattice thermal conductivity is close to the amorphous limit. The origin of the low thermal conductivity has been

debated, but mainly attributed to the interaction between the guest atoms and the cage-type structure. The guest atoms at the 6d site are captured inside the oversized cage and loosely bonded, thus exhibit a large anisotropic atomic displacement parameter, and has been described as rattling atoms.
Previously, the displacement parameter of the guest atom was thought to depend mainly on the cage size, meaning that small guest atoms in the larger cage would exhibit a higher displacement parameter. However, it is found later the rattling nature of guest atoms is more complex, and that the host atom distribution also plays a role. As shown in Figure 5.7, even for the same composition $Ba_8Al_{16}Ge_{30}$, the ADP of the U_{22} direction differs, varying from on-center to off-center positions. In contrast, $Ba_8Ga_{16}Ge_{30}$ shows quite uniform ADP. The different behaviors of the displacement parameter are also observed for the quaternary $Ba_8(Al_xGa_{1-x})_{16}Ge_{30}$, as can be seen in Figure 5.7, the ADP of the U_{22} direction of flux samples increases with x, indicating the Ba atoms are moving away from the center of the cage. On the other hand, sample C-Al5.2 possesses a significantly smaller ADP of the U_{22} direction, meaning the guest atoms are positioned closer to the center of the cages.

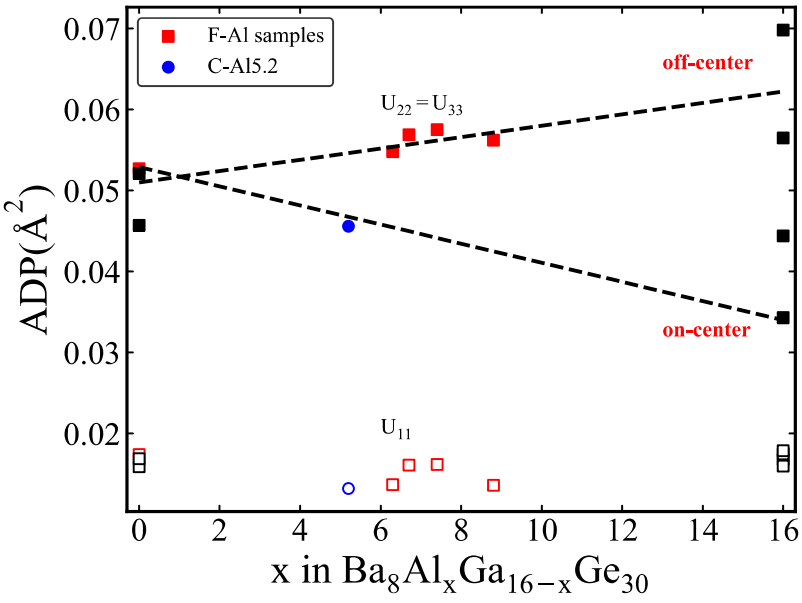

Figure 5.7: *Anisotropic atomic displacement parameter of Ba atoms at the 6d site versus the Al content in* $Ba_8(Al_xGa_{1-x})_{16}Ge_{30}$. *The data is obtained from the single crystal X-ray diffraction at 300 K. The square markers refer to the samples grown by flux method, while the circle markers denote the sample synthesized by Czochralski method. Herein, the filled markers are the ADP at* U_{22} *and* U_{33} *directions, and the unfilled markers are the ADP at* U_{11} *direction. Black markers are the values of reference* $Ba_8Ga_{16}Ge_{30}$ *and* $Ba_8Al_{16}Ge_{30}$ *samples.*

It is desirable to find out the origin of such different behaviors of the displacement parameter. The lattice parameter increases linearly with the value of x, as shown in Figure 5.5, which means that the volume of the large tetrakaidecahedral cage also increases with the amount of Al. If, accordingly, the cage size is the determining factor, one would expect that the displacement parameter for the sample C-Al5.2 should be larger than the sample F-Al0.0, but this is not observed.
The displacement parameter of the Ba atoms reflects the bonding environment: if loosely bonded, the Ba atoms show large displacement parameter, and vice versa. The chemical bonds between guest and host atoms in clathrates are usually considered as ionic, based on the Zintl concept. Thus, the electronegativity of the two atoms bonding together affects the ionic bond energy, consequently the Al-Ba bond is stronger than the Ga-Ba bond. From the analysis of chemical ordering, it is already revealed that the C-Al5.2 sample has a higher Al occupation at the 6c site, so the bonding energy between host and guest atoms in the C-Al5.2 sample is also higher than that in the flux grown samples. As a result, the Ba atoms are located at the on-center position for the C-Al5.2 sample, while for the flux grown samples guest atoms are loosely bonded and showing large displacement parameter.

6 Conclusion and Future Work

The structure of type-I clathrate $Ba_8(Al_xGa_{1-x})_{16}Ge_{30}$ and its effect on the thermoelectric properties are investigated in this thesis.
At microscale level, the thermoelectric performance of $Ba_8Ga_{16}Ge_{30}$ has been improved through modulation doping, achieved by alloying 25 at. % $Ba_8Al_{16}Ge_{30}$ with 75 at. % $Ba_8Ga_{16}Ge_{30}$, which results in a largely improved carrier mobility exceeding that of a single crystal with the same composition. This yields an improved electrical conductivity without decreasing the Seebeck coefficient, achieving the highest reported power factor among sintered type-I clathrate compounds. Microscopy reveals that the materials are composed of a Ga-rich clathrate matrix phase, and Al particles, which aggregate on the grain boundaries or inside the grains. As a result, the highest zT is achieved for samples $Ba_8(Al_xGa_{1-x})_{16}Ge_{30}$ (x = 0.23 and 0.25) with values of 0.99 and 0.93, respectively at 800 °C.
The atomic structure of single crystal $Ba_8(Al_xGa_{1-x})_{16}Ge_{30}$ is investigated by the combination of X-ray and neutron diffraction. The obtained site occupation is validated by, and consistent with theoretical calculations. It is found that Al does not affect the atomic distribution of Ge, but only substitutes Ga in the unit cell. A random occupation of Al is found at the 16i and 24k sites, but at the 6c site the occupation of Al differs depending on the synthesis methods. In addition, the displacement parameter of the Ba atoms in the larger tetrakaidecahedral cages is related to the chemical ordering. They are either localized at the center of the cage or moving towards the boundary of cage periphery.
The future work would focus on two aspects. We have explored the modulation doping and found it achievable in clathrate compounds, by alloying an analogous compound with the matrix phase. It would be even more beneficial to use this methodology for other systems characterized by a larger Seebeck coefficient and a poorer electrical conductivity, in order to boost the carrier mobility. In addition, the chemical ordering of type-I clathrates at the room temperature is examined. However, the structure at high temperature is still unclear, and its impact on the thermoelectric properties has not been scrutinized yet. From the theoretical calculations, there might be an order - disorder phase transition at high temperature for $Ba_8(Al_xGa_{1-x})_{16}Ge_{30}$. Therefore, it is worth trying in-situ high temperature X-ray or neutron diffraction on these materials.

Acknowledgments

The funding from the Swedish Foundation for Strategic Research (SSF) through the Swedish national graduate school in neutron scattering (SwedNess) is gratefully acknowledged.

I would like to thank my supervisor, Anders Palmqvist for giving me the opportunity to start my PhD path. Thanks for always being open minded and the attitude towards the improvement and scrutinization of the research.

Thanks to my collaborators Joakim Brorsson, Ren Qiu, prof. Paul Erhart, prof. Takashi Kamiyama and others helping me with the project, without you the work in this thesis could not have been done.

Specially thanks to Joakim Brorsson, Andrey Sizov and Samul Fretz, for tutoring me in the beginning of my PhD path.

Thanks to my colleagues in the research group: Caroline, Andrey, Gunnar, Joakim, Giulio, Milene, Sam, Sanna and Walter, and all the colleagues in the Applied Chemistry Division. Thank you all for the amazing time.

Finally, thanks to all my friends and my family for everything. Thank my wife Shuxin Zheng for the support, along this long path to the PhD.

References

[1] International Energy Agency `https://https://www.iea.org/`.

[2] Bell, L. E. Cooling, heating, generating power, and recovering waste heat with thermoelectric systems.*Science* **2008**, *321*, 1457–1461.

[3] Snyder, G. J.; Toberer, E. S. Complex thermoelectric materials.*Nature Materials* **2008**, *7*, 105–114.

[4] Pan, Y.; Aydemir, U.; Grovogui, J. A.; Witting, I. T.; Hanus, R.; Xu, Y.; Wu, J.; Wu, C.-F.; Sun, F.-H.; Zhuang, H.-L., et al. Melt-Centrifuged (Bi, Sb) 2Te3: Engineering Microstructure toward High Thermoelectric Efficiency.*Advanced Materials* **2018**, *30*, 1802016.

[5] Li, J.-F.; Liu, W.-S.; Zhao, L.-D.; Zhou, M. High-performance nanostructured thermoelectric materials.*NPG Asia Materials* **2010**, *2*, 152–158.

[6] Biswas, K.; He, J.; Blum, I. D.; Wu, C.-I.; Hogan, T. P.; Seidman, D. N.; Dravid, V. P.; Kanatzidis, M. G. High-performance bulk thermoelectrics with all-scale hierarchical architectures.*Nature* **2012**, *489*, 414–418.

[7] Zhu, G.; Lee, H; Lan, Y.; Wang, X.; Joshi, G; Wang, D.; Yang, J; Vashaee, D; Guilbert, H; Pillitteri, A, et al. Increased phonon scattering by nanograins and point defects in nanostructured silicon with a low concentration of germanium.*Physical Review Letters* **2009**, *102*, 196803.

[8] Beretta, D.; Neophytou, N.; Hodges, J. M.; Kanatzidis, M. G.; Narducci, D.; Martin-Gonzalez, M.; Beekman, M.; Balke, B.; Cerretti, G.; Tremel, W., et al. Thermoelectrics: From history, a window to the future.*Materials Science and Engineering: R: Reports* **2019**, *138*, 100501.

[9] Voyager - Mission Status `https://voyager.jpl.nasa.gov/mission/status/#sfos`.

[10] He, J.; Tritt, T. M. Advances in thermoelectric materials research: Looking back and moving forward.*Science* **2017**, *357*.

[11] Kauzlarich, S. M.; Brown, S. R.; Snyder, G. J. Zintl phases for thermoelectric devices.*Dalton Transactions* **2007**, 2099–2107.

[12] Christensen, M.; Johnsen, S.; Iversen, B. B. Thermoelectric clathrates of type I.*Dalton Transactions* **2010**, *39*, 978–992.

[13] Takabatake, T.; Suekuni, K.; Nakayama, T.; Kaneshita, E. Phonon-glass electron-crystal thermoelectric clathrates: Experiments and theory.*Reviews of Modern Physics* **2014**, *86*, 669.

[14] Dolyniuk, J.-A.; Owens-Baird, B.; Wang, J.; Zaikina, J. V.; Kovnir, K. Clathrate thermoelectrics.*Materials Science and Engineering: R: Reports* **2016**, *108*, 1–46.

[15] Rowe, D. M., *CRC HANDBOOK of thermoelectrics*; CRC Press: Boca Raton; New York; London, 1995.

[16] Heremans, J. P.; Jovovic, V.; Toberer, E. S.; Saramat, A.; Kurosaki, K.; Charoenphakdee, A.; Yamanaka, S.; Snyder, G. J. Enhancement of thermoelectric efficiency in PbTe by distortion of the electronic density of states.*Science* **2008**, *321*, 554–557.

[17] Pei, Y.; Shi, X.; LaLonde, A.; Wang, H.; Chen, L.; Snyder, G. J. Convergence of electronic bands for high performance bulk thermoelectrics.*Nature* **2011**, *473*, 66–69.

[18] Xie, H.; Wang, H.; Fu, C.; Liu, Y.; Snyder, G. J.; Zhao, X.; Zhu, T. The intrinsic disorder related alloy scattering in ZrNiSn half-Heusler thermoelectric materials.*Scientific Reports* **2014**, *4*, 6888.

[19] Kittel, C.; McEuen, P.; McEuen, P., *Introduction to solid state physics*; Wiley New York: 1996; Vol. 8.

[20] Ma, Y.; Heijl, R.; Palmqvist, A. E. Composite thermoelectric materials with embedded nanoparticles.*Journal of Materials Science* **2013**, *48*, 2767–2778.

[21] Koza, M. M.; Johnson, M. R.; Viennois, R.; Mutka, H.; Girard, L.; Ravot, D. Breakdown of phonon glass paradigm in La-and Ce-filled Fe 4 Sb 12 skutterudites.*Nature Materials* **2008**, *7*, 805–810.

[22] Iversen, B. B.; Palmqvist, A. E.; Cox, D. E.; Nolas, G. S.; Stucky, G. D.; Blake, N. P.; Metiu, H. Why are clathrates good candidates for thermoelectric materials?*Journal of Solid State Chemistry* **2000**, *149*, 455–458.

[23] Sales, B. C.; Chakoumakos, B.; Jin, R; Thompson, J.; Mandrus, D Structural, magnetic, thermal, and transport properties of X 8 Ga 16 Ge 30 (X= E u, S r, Ba) single crystals.*Physical Review B* **2001**, *63*, 245113.

[24] Blake, N. P.; Latturner, S.; Bryan, J. D.; Stucky, G. D.; Metiu, H. Band structures and thermoelectric properties of the clathrates Ba 8 Ga 16 Ge 30, Sr 8 Ga 16 Ge 30, Ba 8 Ga 16 Si 30, and Ba 8 In 16 Sn 30.*The Journal of Chemical Physics* **2001**, *115*, 8060–8073.

[25] Snyder, G. J.; Christensen, M.; Nishibori, E.; Caillat, T.; Iversen, B. B. Disordered zinc in Zn 4 Sb 3 with phonon-glass and electron-crystal thermoelectric properties.*Nature Materials* **2004**, *3*, 458–463.

[26] Wang, J.; Wang, L.-L.; Kovnir, K. Phonon glass behavior beyond traditional cage structures: synthesis, crystal and electronic structure, and properties of KMg 4 Sb 3.*Journal of Materials Chemistry A* **2018**, *6*, 4759–4767.

[27] Zhao, L.-D.; Lo, S.-H.; Zhang, Y.; Sun, H.; Tan, G.; Uher, C.; Wolverton, C.; Dravid, V. P.; Kanatzidis, M. G. Ultralow thermal conductivity and high thermoelectric figure of merit in SnSe crystals.*Nature* **2014**, *508*, 373–377.

[28] Li, C. W.; Hong, J.; May, A. F.; Bansal, D.; Chi, S.; Hong, T.; Ehlers, G.; Delaire, O Orbitally driven giant phonon anharmonicity in SnSe.*Nature Physics* **2015**, *11*, 1063–1069.

[29] Dong, J.; Sun, F.-H.; Tang, H.; Pei, J.; Zhuang, H.-L.; Hu, H.-H.; Zhang, B.-P.; Pan, Y.; Li, J.-F. Medium-temperature thermoelectric GeTe: vacancy suppression and band structure engineering leading to high performance.*Energy & Environmental Science* **2019**, *12*, 1396–1403.

[30] Pei, Y.; Tan, G.; Feng, D.; Zheng, L.; Tan, Q.; Xie, X.; Gong, S.; Chen, Y.; Li, J.-F.; He, J., et al. Integrating band structure engineering with all-scale hierarchical structuring for high thermoelectric performance in PbTe system.*Advanced Energy Materials* **2017**, *7*, 1601450.

[31] Schäffler, F. High-mobility Si and Ge structures.*Semiconductor Science and Technology* **1997**, *12*, 1515.

[32] Dingle, R; Störmer, H.; Gossard, A.; Wiegmann, W Electron mobilities in modulation-doped semiconductor heterojunction superlattices.*Applied Physics Letters* **1978**, *33*, 665–667.

[33] Zebarjadi, M.; Joshi, G.; Zhu, G.; Yu, B.; Minnich, A.; Lan, Y.; Wang, X.; Dresselhaus, M.; Ren, Z.; Chen, G. Power factor enhancement by modulation doping in bulk nanocomposites.*Nano Letters* **2011**, *11*, 2225–2230.

[34] Yu, B.; Zebarjadi, M.; Wang, H.; Lukas, K.; Wang, H.; Wang, D.; Opeil, C.; Dresselhaus, M.; Chen, G.; Ren, Z. Enhancement of thermoelectric properties by modulation-doping in silicon germanium alloy nanocomposites.*Nano Letters* **2012**, *12*, 2077–2082.

[35] Pei, Y.-L.; Wu, H.; Wu, D.; Zheng, F.; He, J. High thermoelectric performance realized in a BiCuSeO system by improving carrier mobility through 3D modulation doping.*Journal of the American Chemical Society* **2014**, *136*, 13902–13908.

[36] Wu, D.; Pei, Y.; Wang, Z.; Wu, H.; Huang, L.; Zhao, L.-D.; He, J. Significantly enhanced thermoelectric performance in n-type heterogeneous BiAgSeS composites.*Advanced Functional Materials* **2014**, *24*, 7763–7771.

[37] Yamini, S. A.; Mitchell, D. R.; Gibbs, Z. M.; Santos, R.; Patterson, V.; Li, S.; Pei, Y. Z.; Dou, S. X.; Jeffrey Snyder, G Heterogeneous Distribution of Sodium for High Thermoelectric Performance of p-type Multiphase Lead-Chalcogenides.*Advanced Energy Materials* **2015**, *5*, 1501047.

[38] Berry, T.; Fu, C.; Auffermann, G.; Fecher, G. H.; Schnelle, W.; Serrano-Sanchez, F.; Yue, Y.; Liang, H.; Felser, C. Enhancing thermoelectric performance of TiNiSn half-Heusler compounds via modulation doping.*Chemistry of Materials* **2017**, *29*, 7042–7048.

[39] Wang, J.; Zhang, B.-Y.; Kang, H.-J.; Li, Y.; Yaer, X.; Li, J.-F.; Tan, Q.; Zhang, S.; Fan, G.-H.; Liu, C.-Y., et al. Record high thermoelectric performance in bulk SrTiO3 via nano-scale modulation doping.*Nano Energy* **2017**, *35*, 387–395.

[40] Neophytou, N.; Thesberg, M. Modulation doping and energy filtering as effective ways to improve the thermoelectric power factor.*Journal of Computational Electronics* **2016**, *15*, 16–26.

[41] Bentien, A.; Christensen, M; Bryan, J.; Sanchez, A; Paschen, S; Steglich, F; Stucky, G.; Iversen, B. Thermal conductivity of thermoelectric clathrates.*Physical Review B* **2004**, *69*, 045107.

[42] Avila, M.; Suekuni, K.; Umeo, K.; Fukuoka, H.; Yamanaka, S.; Takabatake, T. Glasslike versus crystalline thermal conductivity in carrier-tuned Ba 8 Ga 16 X 30 clathrates (X= Ge, Sn).*Physical Review B* **2006**, *74*, 125109.

[43] Christensen, M.; Lock, N.; Overgaard, J.; Iversen, B. B. Crystal structures of thermoelectric n-and p-type Ba8Ga16Ge30 studied by single crystal, multitemperature, neutron diffraction, conventional X-ray diffraction and resonant synchrotron X-ray diffraction.*Journal of the American Chemical Society* **2006**, *128*, 15657–15665.

[44] Christensen, M.; Abrahamsen, A. B.; Christensen, N. B.; Juranyi, F.; Andersen, N. H.; Lefmann, K.; Andreasson, J.; Bahl, C. R.; Iversen, B. B. Avoided crossing of rattler modes in thermoelectric materials.*Nature Materials* **2008**, *7*, 811–815.

[45] Chen, C.; Zhang, Z.; Chen, J. Revisit to the impacts of rattlers on thermal conductivity of clathrates.*Frontiers in Energy Research* **2018**, *6*, 34.

[46] Lindroth, D. O.; Brorsson, J.; Fransson, E.; Eriksson, F.; Palmqvist, A.; Erhart, P. Thermal conductivity in intermetallic clathrates: A first-principles perspective.*Physical Review B* **2019**, *100*, 045206.

[47] Shi, X.; Yang, J.; Bai, S.; Yang, J.; Wang, H.; Chi, M.; Salvador, J. R.; Zhang, W.; Chen, L.; Wong-Ng, W. On the design of high-efficiency thermoelectric clathrates through a systematic cross-substitution of framework elements.*Advanced Functional Materials* **2010**, *20*, 755–763.

[48] Cederkrantz, D.; Saramat, A.; Snyder, G. J.; Palmqvist, A. Thermal stability and thermoelectric properties of p-type Ba 8 Ga 16 Ge 30 clathrates. *Journal of Applied Physics* **2009**, *106*, 074509.

[49] Manière, C.; Durand, L.; Weibel, A.; Estournès, C. Spark-plasma-sintering and finite element method: From the identification of the sintering parameters of a submicronic α-alumina powder to the development of complex shapes. *Acta Materialia* **2016**, *102*, 169–175.

[50] Guillon, O.; Gonzalez-Julian, J.; Dargatz, B.; Kessel, T.; Schierning, G.; Räthel, J.; Herrmann, M. Field-assisted sintering technology/spark plasma sintering: mechanisms, materials, and technology developments. *Advanced Engineering Materials* **2014**, *16*, 830–849.

[51] Giuntini, D.; Olevsky, E. A.; Garcia-Cardona, C.; Maximenko, A. L.; Yurlova, M. S.; Haines, C. D.; Martin, D. G.; Kapoor, D. Localized overheating phenomena and optimization of spark-plasma sintering tooling design. *Materials* **2013**, *6*, 2612–2632.

[52] Yucheng, W.; Zhengyi, F.; Weimin, W.; Jinyong, Z. Numerical simulation of the temperature field in sintering of TiB 2-BN by SPS. *Journal of Wuhan University of Technology-Mater. Sci. Ed.* **2006**, *21*, 126–128.

[53] Gustafsson, S. E. Transient plane source techniques for thermal conductivity and thermal diffusivity measurements of solid materials. *Review of Scientific Instruments* **1991**, *62*, 797–804.

[54] Wang, J.; Lebedev, O. I.; Lee, K.; Dolyniuk, J.-A.; Klavins, P.; Bux, S.; Kovnir, K. High-efficiency thermoelectric Ba 8 Cu 14 Ge 6 P 26: bridging the gap between tetrel-based and tetrel-free clathrates. *Chemical Science* **2017**, *8*, 8030–8038.

[55] Dolyniuk, J.-A.; Wang, J.; Marple, M. A.; Sen, S.; Cheng, Y.; Ramirez-Cuesta, A. J.; Kovnir, K. Chemical Bonding and Transport Properties in Clathrates-I with Cu–Zn–P Frameworks. *Chemistry of Materials* **2018**, *30*, 3419–3428.

[56] Wang, J.; Dolyniuk, J.-A.; Kovnir, K. Unconventional clathrates with transition metal–phosphorus frameworks. *Accounts of Chemical Research* **2018**, *51*, 31–39.

[57] Yan, X.; Ikeda, M.; Zhang, L.; Bauer, E.; Rogl, P.; Giester, G.; Prokofiev, A.; Paschen, S. Suppression of vacancies boosts thermoelectric performance in type-I clathrates. *Journal of Materials Chemistry A* **2018**, *6*, 1727–1735.

[58] Zhang, Y.; Wilkinson, A. P.; Nolas, G. S.; Lee, P. L.; Hodges, J. P. Strategies for solving neighboring-element problems: a case study using resonant X-ray diffraction and pulsed neutron diffraction to examine Sr8Ga16Ge30. *Journal of Applied Crystallography* **2003**, *36*, 1182–1189.

Appended Papers